Environmental Industry Letters
https://journals.tultech.eu/index.php/eil
ISSN: 2806-2965
Volume 3, Issue 2
DOI: https://doi.org/10.15157/EIL.2025.3.2.68-112
Received: 12.09.2025; Revised: 03.11.2025; Accepted: 19.12.2025

Enhancing Material Efficiency in Seismic-Resistant Reinforced Concrete Columns: A Sustainable Analytical Framework Using Axial-Shear-Flexure Interaction and Modified Compression Field Theory

Seyedalireza Mousavi[1], Niloofar Rouhani[2], Meysam Samadi[1], Benyamin Chahkandi[3], Amir M. Fathollahi-Fard[4*], Amirhossein Ahmadi[5]

[1]Department of Civil Engineering, Mashhad Branch, Islamic Azad University, Mashhad, Iran
[2]Department of Civil Engineering, Ferdowsi University of Mashhad, Mashhad, Iran
[3]Faculty of Civil and Environmental Engineering, Gdansk University of Technology, ul. Narutowicza 11/12, 80-233 Gdansk, Poland
[4]School of Business Administration, Laurentian University, 935 Ramsey Lake Road, Sudbury, ON P3E 2C6, Canada
[5]Institute for Nanomaterials, Advanced Technologies and Innovation, Technical University of Liberec, Studentská 1402/2, 461 17 Liberec 1, Czech Republic
***AFathollahiFard@laurentian.ca**

Abstract
Reinforced concrete columns serve an important role in increasing the seismic resilience of buildings. However, modelling their nonlinear response to earthquake-induced loading presents a substantial problem. This research introduces a pioneering approach employing Axial-Shear-Flexure Interaction (ASFI) and Modified Compression Field Theory (MCFT) to anticipate the force-displacement behaviour and failure modes of reinforced concrete columns under lateral cyclic loading. The proposed analytical model undergoes validation against experimental findings from 11 column specimens subjected to increasing drift cycles until failure. Results demonstrate the model's ability to reasonably capture initial stiffness, yield displacement, and the progression of damage, exhibiting a close correlation with the experimental outcomes. Nevertheless, the study highlights certain limitations in simulating the post-yield displacement capacity, particularly for shear-critical columns, where the model tends to overestimate ductility in comparison to experimental tests. Overall, the analytical model displays promising performance and efficiency in evaluating column seismic response without necessitating extensive testing. The findings offer preliminary validation for the effectiveness of ASFI and MCFT-based techniques. The study emphasizes the need for refining material constitutive models and incorporating advanced shear and fracture mechanics to enhance accuracy. This research marks a significant stride toward the development of analytical tools capable of efficiently simulating the intricate nonlinear behaviours of columns under seismic excitations.

Keywords: Reinforced concrete columns; Seismic resilience; Analytical modelling; Axial-Shear-Flexure Interaction (ASFI); Modified Compression Field Theory (MCFT).

INTRODUCTION

A significant proportion of Iranian concrete buildings suffer from inadequate earthquake design, leading to severe damage or collapse during seismic crises [1, 2]. Notably, the prevalent issue in the Iranian building industry is linked to outdated regulations that solely emphasize force considerations, neglecting the critical interplay between force and displacement [3]. In contrast, contemporary international standards advocate for a comprehensive approach, stipulating that structures must possess the capacity to withstand both forces and corresponding displacements [4, 5]. In line with these updated guidelines, the lateral displacement bearing capacity of columns assumes paramount significance in the seismic performance of structures, necessitating a thorough assessment of their ability to endure shear forces and bending [6, 7].

While columns represent crucial elements within modern structures and remain a focus of extensive research, a notable portion of efforts tends to concentrate on statistical methodologies [8]. Conversely, analytical approaches predominantly rely on assumptions about a specific value for the final compressive strain of concrete, leading to various ambiguities [9], which can be even applied to pandemics and post-pandemics environments. For instance, Peruš et al. [10] employed a non-parametric empirical approach to estimate the flexural deformation capacity of reinforced concrete columns, while Tagle et al. [11] conducted a case study involving seismic loading to identify stages of damage. Additionally, Li et al. [12] utilized experimental data to investigate damage distributions in the plastic hinge zone, while Marder et al. [13] conducted tests involving both cyclic and earthquake-type loading to examine residual cracks. Using a hybrid approach based on the Gaussian model and the genetic algorithm.

Undoubtedly, significant efforts have been devoted to evaluating the lateral displacement and overall seismic behaviour of columns. However, many existing methodologies rely on statistical analyses, empirical investigations, or isolated mathematical calculations [14]. Reinforced concrete (RC) columns subjected to reversed cyclic loading exhibit complex nonlinear behaviour driven by the interplay of flexural, shear, and axial mechanisms [15]. In practical terms, axial-shear-flexural interaction refers to the simultaneous and interdependent action of axial load, shear force, and flexural demand in RC columns during seismic loading. Axial load alters the compression state of concrete and affects both stiffness and drift capacity; flexure controls curvature development, crack localization, and plastic hinge formation; and shear governs diagonal cracking, stiffness degradation, and possible brittle failure. In real columns, these mechanisms develop together rather than independently. As a result, a change in axial load level or shear demand can significantly modify flexural response, lateral displacement capacity, and the governing failure mode. Initially, flexural cracking occurs in the tensile zones near the column ends under moderate lateral loads. As loading progresses, these cracks localize at the ends, forming plastic hinges characterized by significant concrete spalling and rebar buckling. In shear-critical columns, insufficient transverse reinforcement results in diagonal inclined cracks, which can lead to brittle shear failure. Columns experiencing combined axial-shear-flexure interaction demonstrate even more intricate failure patterns, including simultaneous flexural cracking, shear stress concentration, and axial capacity loss, which may culminate in collapse under high axial load ratios. Crack patterns vary depending on the failure mode: flexure-dominated columns exhibit vertical cracks, shear-dominated columns show diagonal cracks, and combined modes display a mix of both patterns.

Practical guidelines, such as ASCE-41 and its predecessors FEMA-356 and FEMA-440, provide empirical frameworks for estimating the plastic rotation capacity of RC columns [16, 17]. These guidelines consider critical parameters, including axial load ratio, shear demand, and reinforcement ratios, to characterize column behaviour under seismic conditions. For instance, higher axial load ratios reduce drift capacity by intensifying compressive stress, while increased shear demand can cause premature shear failures, especially in poorly confined columns. Longitudinal and transverse reinforcement ratios also play significant roles in influencing ductility and failure modes, with transverse reinforcement resisting shear forces and limiting crack propagation. However, these empirical methods rely on simplified assumptions and relationships that often fail to accurately capture the complex interactions among axial, shear, and flexural mechanisms.

Recent analytical studies have advanced the nonlinear modelling of non-ductile RC columns by explicitly incorporating shear-flexure interaction into frame-element formulations. Sae-Long et al. [18] developed a nonlinear frame element for seismic analysis of non-ductile RC columns that accounted for spread inelasticity, shear-flexure coupling, and shear-strength deterioration. Sae-Long et al. [19] later extended this approach into a force-based formulation to improve computational efficiency and representation of flexure-shear-critical column behaviour. Sae-Long et al. [20] further expanded the framework to members interacting with supporting media through a nonlinear Winkler-based foundation model. The formulation was subsequently refined by including bond-slip effects in the shear-flexure-interaction element, which improved simulation of the shear response in non-ductile RC columns under seismic loading. Later developments extended the same modelling philosophy to more advanced foundation representations, including Kerr-type and Winkler-Pasternak foundation models [21, 22]. Although these studies significantly improved the mechanics-based simulation of shear-flexure interaction in RC members, their main focus remained on frame-element development and foundation effects. In contrast, the present study focuses on direct prediction of the lateral force-displacement response and failure behaviour of RC columns by coupling ASFI with MCFT under cyclic loading.

However, the limitations of the building codes, especially in the local region stem from their reliance on outdated methodologies that prioritize force considerations over displacement and deformation requirements [23]. Similar shortcomings are observed in the seismic design codes of other regions, which often struggle to address the complexities of nonlinear behaviour in existing reinforced concrete structures under seismic loads. For example, the American code ASCE-41 adopts a performance-based approach but depends on empirical formulations for plastic rotation capacity and assumes simplified material behaviour, leading to inaccuracies in highly nonlinear scenarios. European codes, such as Eurocode 8, primarily focus on new constructions and provide limited guidance for assessing existing structures with poor detailing or inadequate confinement.

Additionally, while codes in regions such as Japan and New Zealand are advanced in addressing ductility demands, they may not comprehensively account for the interaction between axial, shear, and flexural forces in older buildings, particularly under severe cyclic loading [24, 25].

These limitations hinder accurate prediction of post-yield behaviour and failure modes, especially in shear-critical columns or structures with irregular configurations.

To overcome these challenges, this study proposes a novel analytical framework integrating axial-shear-flexure interaction (ASFI) and the Modified Compression Field Theory (MCFT). Unlike conventional approaches, the proposed model captures critical phenomena such as localized shear cracking, progressive concrete crushing, and rebar buckling. This integration provides a more accurate representation of post-yield behaviour and ductility, addressing key limitations of existing codes and guidelines.

Consequently, it becomes evident that a research gap exists in establishing a robust and comprehensive framework for identifying the lateral displacement of reinforced concrete columns. Given that a column's seismic behaviour is the culmination of bending mechanisms, rebar slippage, and shear forces, this study aims to address the aforementioned research gap by pursuing , compilation of experimental data on final bending and shear deformation, application of the Axial-Shear-Flexure Interaction (ASFI) and Modified Compression Field Theory (MCFT) to predict Axial-Shear-Flexure deformation, implementation of a Mathematica program to compute lateral displacement, comparative analysis of the proposed methods with experimental findings. The prediction model proposed in this study introduces a novel approach to modelling the behaviour of RC columns under cyclic loading by integrating ASFI with the MCFT. While previous studies have incorporated shear-flexure interaction into nonlinear frame formulations, a robust framework for directly predicting the lateral force-displacement response and failure behaviour of RC columns through coupling of ASFI and MCFT remains limited. This integration is particularly critical for understanding the nonlinear response of RC columns during seismic events, where the interplay among these mechanisms dictates structural performance and failure modes.

A key novelty of the present study lies in advancing beyond the conventional reliance on empirical relationships and simplified assumptions that have historically limited the fidelity of such models. Many prior approaches such as Elwood [26], used empirical shear formulations or focused primarily on strength-based criteria, often neglecting the complex interaction between shear, axial, and flexural behaviours throughout the deformation process. The present model introduces significant refinements by explicitly integrating the MCFT, a principal stress-based, mechanics-grounded shear model—into the ASFI spring-based framework. This integration enables a more accurate simulation of shear deformation, incorporating critical nonlinear effects such as compression softening and tension stiffening, which are especially relevant near failure. Unlike earlier models that primarily target failure initiation, our approach tracks the continuous evolution of shear, flexural, and reinforcement slip deformations throughout the entire loading history. Moreover, this study uniquely addresses localized failure phenomena, such as progressive shear cracking, concrete crushing, and rebar buckling, which are typically overlooked in traditional models. By explicitly incorporating these effects through carefully calibrated stress-strain relationships and equilibrium-based coupling of shear and flexure, the model provides a more realistic prediction of post-yield behaviour and failure mechanisms. Finally, by structuring the computational procedure within ASFI, we overcome the inherent complexity of applying MCFT in isolation, making the model both accurate and practically usable for modern performance-based seismic design.

The main objective of this study is to develop and validate a coupled ASFI-MCFT analytical model for predicting the nonlinear seismic response, deformation components, and failure behaviour of reinforced concrete columns subjected to cyclic lateral loading. The scope of this study is limited to the analytical prediction of the lateral force-displacement response and failure behaviour of reinforced concrete columns under cyclic lateral loading through coupling of ASFI and MCFT. The framework is validated using 11 experimentally tested column specimens selected from the literature with sufficiently complete data. The present study does not aim to provide a universal model for all column types and loading conditions. Its limitations include the relatively small validation dataset, simplified representation of progressive deterioration mechanisms such as bond-slip, localized shear cracking, concrete crushing, and rebar buckling, and reduced accuracy in the post-yield range, particularly for shear-critical columns. The rest of this paper is organized as follows: Section 2 outlines the materials and methods utilized, encompassing the research methodology, case study, and the analytical modelling approach adopted. In Section 3, we present our computed results and engage in a comprehensive discussion of our findings. Finally, Section 4 serves as the conclusion, encapsulating the key insights of this study, along with suggestions for potential avenues for future research.

MATERIAL AND METHODS

Here, we initially establish the research methodology applied in this study, followed by a comprehensive overview of our case study conducted in Iran. Subsequently, we present the final displacement values derived from our ASFI and MCFT methods. Further, we provide our ultimate estimations for the variables under consideration. Lastly, we expand and elaborate on the overarching solution algorithm in detail.

Research methodology

The primary objective of this study is to propose a framework for designing structurally robust and resilient buildings that exhibit optimal behaviour during seismic events. Considering the findings from the literature review, it is evident that columns significantly impact the seismic potential of reinforced concrete structures. Consequently, accurately predicting the load-deformation response of columns within a building becomes imperative.

The proposed analytical framework is grounded in the mechanical principles ASFI and MCFT. These methods explicitly model the interplay of axial loads, flexural deformations, and shear stresses, capturing the nonlinear behaviour of reinforced concrete columns under cyclic loading. ASFI integrates axial-shear and flexural effects by superimposing their respective contributions to displacement and strain. MCFT extends this approach by incorporating rotating crack models, tension stiffening effects, and compression softening behaviour, allowing accurate simulation of critical failure modes. MCFT offers advanced modelling of shear behaviour, capturing key effects such as rotating cracks, compression softening, and tension stiffening. By embedding MCFT into ASFI's spring-based structure, which also accounts for flexural and reinforcement slip deformations, the framework enables a precise calculation of total lateral displacement. The combination ensures compatibility between shear and flexure through enforced stress equilibrium, improving the accuracy of predicting failure modes. Importantly, it allows tracking the evolution of deformation mechanisms across the entire loading process, producing results that closely match experimental observations. Moreover, ASFI streamlines the computational complexity of MCFT, providing engineers with a practical and unified tool for performance-based design and seismic evaluation of reinforced concrete columns.

The proposed model is based on several key assumptions to balance computational efficiency with accuracy in capturing the complex behaviour of reinforced concrete columns under cyclic loading. It assumes that plane sections remain plane under deformation, ensuring compatibility between axial and flexural strains and accurately modelling flexural behaviour. Shear cracks are assumed to propagate uniformly within defined critical regions, such as plastic hinges or areas with high shear demand, to simplify the representation of crack patterns while capturing their influence on column behaviour. Additionally, the constitutive material models for concrete and reinforcement account for their nonlinear stress-strain relationships, incorporating strain-hardening in steel reinforcement and strain-softening in concrete to effectively represent the progressive damage and plasticity observed during seismic events. These assumptions provide a robust framework for modelling the coupled effects of axial, shear, and flexural forces.

The study involves a comprehensive comparison between experimental and predicted results, encompassing various forms of deformation such as bending and shear interaction, pressure bar buckling, and displacement attributed to rebar slippage. Rebar buckling was considered by incorporating separate stress-strain relationships for compression steel, modified to account for post-buckling degradation. These relationships were derived from experimental data [27], reflecting the effects of geometric factors like bar diameter and stirrup spacing. The model tracks when compressive strain reaches a critical buckling level, after which the reduced stress capacity from the post-buckling curve is applied in the analysis, allowing accurate prediction of post-peak behaviour and ultimate displacement. Figure 1 illustrates the research roadmap employed in this study, outlining the specific methods utilized at each step.

The analytical method in this study accounts for cyclic effects by employing the MCFT and the ASFI model, which together address the complex interactions that occur during cyclic loading. The MCFT component is particularly instrumental in simulating shear behaviour under cyclic loads, while the ASFI model is used to capture the combined axial, shear, and flexural responses. The convergence iteration process allows for the continuous adjustment of shear and axial stress across different cycles, effectively capturing the degradation of stiffness and strength under repeated loading. This iterative process serves as an inherent correction mechanism to simulate cyclic degradation effects without the need for additional correction factors. This approach helps in accounting for stiffness degradation and changes in force-displacement behaviour typically observed in reinforced concrete columns under cyclic loading conditions.

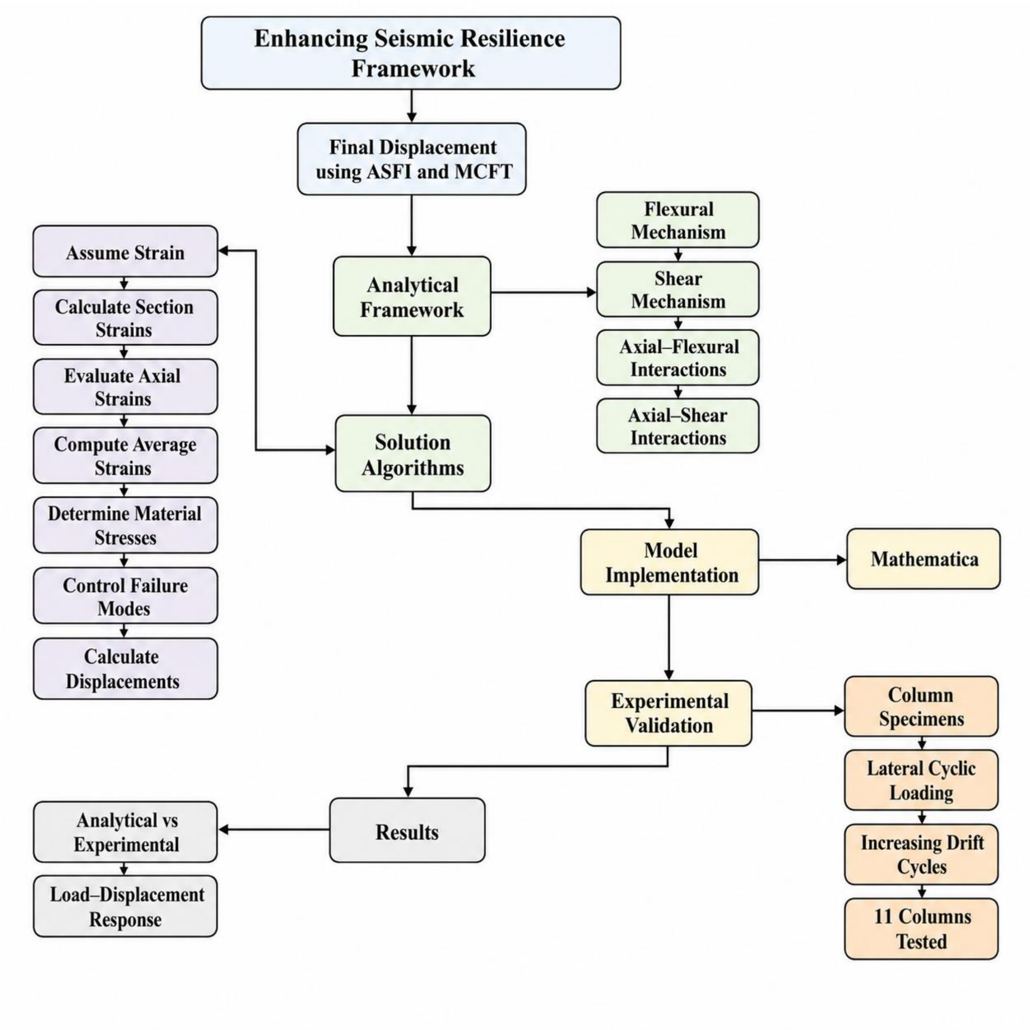

Figure 1. Research roadmap in this study

The basic principle of prediction models is based on coupling the ASFI model with the MCFT to simulate the complex behaviour of reinforced concrete columns under lateral loads. The ASFI model aims to predict the combined influence of axial force, shear, and flexural effects on column deformation. The fundamental assumption here is that these effects interact nonlinearly, especially under cyclic loading conditions. The governing equation for axial-flexural interaction can be represented as Eq (1) [28]:

$$M = \int f_c \cdot z \cdot dA_c = \Sigma A_s \left(f_{s\text{-crack}} - f_{s\text{-average}}\right) \cdot z_s \tag{1}$$

where M is the moment, f_c is the average concrete tensile stress, z is the distance from the neutral axis to a given fiber, dAc is the differential element of cracked concrete area, As is the steel reinforcement area, $f_{s\text{-}crack}$ and $f_{s\text{-}average}$ are the local (at-crack) and average steel stresses, and z_s is the distance from the neutral axis to the steel layer. This relationship illustrates how the moment carried by the average concrete tension across the cracked section must balance the moment from the mismatch between local and average steel stress, linking the section's flexural equilibrium to strain compatibility at the crack.

The MCFT is employed to model shear behaviour, accounting for factors like compression softening and tension stiffening effects, which are significant in concrete elements under lateral loads. MCFT calculations are carried out in the principal stress space, which allows for an accurate representation of the cracked concrete's response under load. The principal stresses (f1, ,f2) are used to compute the shear stress (τ) through the following Eq. (2) [29]:

$$f_{cx} = f_{c1} - v_{cxy}/\tan\theta_c,\ f_{cy} = f_{c1} - v_{cxy}\cdot\tan\theta_c,\ f_{c2} = f_{c1} - v_{cxy}\cdot(\tan\theta_c + 1/\tan\theta_c) \rightarrow \text{setting } f\_cy = 0 \text{ in and rearranging} \rightarrow \tau = f_1\cdot\cot(\theta) \quad (2)$$

where θ is the principal stress angle. The MCFT's contribution ensures that the impact of shear is fully integrated into the model's predictions, thus capturing the combined effect of axial, shear, and flexural actions effectively. By coupling ASFI and MCFT, the prediction model offers a holistic view of the column behaviour, taking into consideration the interactions between different load effects. This coupled approach allows the model to simulate not only the pre-cracking behaviour but also post-cracking and post-yield behaviour, providing a comprehensive analysis of column deformation under seismic loading.

Case study

The samples in this study are picked from another solid research to have a strong frame of reference, drawn from five experimental programs: Soesianawati et al. [30], Zahn et al. [31], Tanaka and Tanaka and Park [32], Watson et al. [33], and Xiao and Martirossyan [34]. The eleven samples and their characteristics are depicted in Table 1 as well as the strain values of compressive and tensile steels which are illustrated in Table 2. The strain values presented in Table 2 are measured values extracted from experimental tests conducted by the respective authors of the original studies. The selection of older but comprehensively documented specimens ensures rigorous benchmarking of the analytical model across diverse failure modes. The chosen tests allow clear separation of shear, flexural, and axial behaviours, which is indispensable for validating the ASFI-MCFT coupled framework. Although newer experimental tests exist, they often lack such fine-grained component-level data, which remains crucial for the objectives of this study. Future work will aim to include more recent datasets as measurement technologies advance.

Table 1. Characteristics of the samples in the current study.

Samples	P (kN)	f_c (MPa)	f_{co} (MPa)	ρ_s	A_s (mm²)	A_s' (mm²)	d_b (mm)	Cover (mm)	B=H (mm)	d (mm)	d' (mm)
Soesianawati et al. **[30]**	744000	46.5	68.19091	0.0151	1208	1208	16	13	400	379	21

Soesianawati et al. **[30]**	2112000	44	66.3325	0.0151	1208	1208	16	13	400	379	21
Soesianawati et al. **[30]**	2112000	44	66.3325	0.0151	1208	1208	16	13	400	379	21
Soesianawati et al. **[30]**	1920000	40	63.24555	0.0151	1208	1208	16	13	400	379	21
Zahn et al. **[31]**	1010000	28.3	53.19774	0.0151	1208	1208	16	13	400	379	21
Zahn et al. **[31]**	2502000	40.1	63.32456	0.0151	1208	1208	16	13	400	379	21
Tanaka and Park **[32]**	819000	25.6	50.59644	0.0157	1256	1256	20	40	400	350	50
Watson et al. **[33]**	3200000	40	63.24555	0.0151	1208	1208	16	13	400	379	21
Watson et al. **[33]**	4704000	42	64.80741	0.0151	1208	1208	16	13	400	379	21
Watson et al. **[33]**	4368000	38	61.64414	0.0151	1208	1208	16	13	400	379	21
Xiao and Martirossyan **[34]**	489000	76	87.17798	0.0355	1127.196	1127.196	20	13	252	229	23

*As (mm^2): Area of longitudinal reinforcement in tension, As' (mm^2): Area of longitudinal reinforcement in compression, ρ_s, represents the volumetric ratio of transverse reinforcement to the volume of concrete core confined by the reinforcement

Table 2. Strain values of compressive and tensile steels and final curvature of the section in exchange for different values of final compressive strain of concrete.

Specifications			The final strain = 0.006			The final strain = 0.01			The final strain = 0.02		
samples	X(mm)	M(N.mm)	$\emptyset_{ultimate}$	ε_s	ε_s'	$\emptyset_{ultimate}$	ε_s	ε_s'	$\emptyset_{ultimate}$	ε_s	ε_s'
Soesianawati et al. **[30]**	54.55273	3.01E+08	0.00011	0.035684	0.00369	0.000183	0.059474	0.006151	0.000367	0.118948	0.012301
Soesianawati et al. **[30]**	159.198	4.27E+08	3.77E-05	0.008284	0.005209	6.28E-05	0.013807	0.008681	0.000126	0.027614	0.017362
Soesianawati et al. **[30]**	159.198	4.27E+08	3.77E-05	0.008284	0.005209	6.28E-05	0.013807	0.008681	0.000126	0.027614	0.017362
Soesianawati et al. **[30]**	151.7893	4.11E+08	3.95E-05	0.008981	0.00517	6.59E-05	0.014969	0.008617	0.000132	0.029938	0.017233
Zahn et al. **[31]**	94.92884	3.27E+08	6.32E-05	0.017955	0.004673	0.000105	0.029925	0.007788	0.000211	0.059849	0.015576
Zahn et al. **[31]**	197.5537	4.26E+08	3.04E-05	0.005511	0.005362	5.06E-05	0.009185	0.008937	0.000101	0.018369	0.017874
Tanaka and Park **[32]**	80.93454	2.81E+08	7.41E-05	0.019947	0.002293	0.000124	0.033245	0.003822	0.000247	0.06649	0.007644
Watson et al. **[33]**	252.9822	4.08E+08	2.37E-05	0.002989	0.005502	3.95E-05	0.004981	0.00917	7.91E-05	0.009963	0.01834
Watson et al. **[33]**	362.9215	2.60E+08	1.65E-05	0.000266	0.005653	2.76E-05	0.000443	0.009421	5.51E-05	0.000886	0.018843

Watson et al. **[33]**	354.2916	2.73E+08	1.69E-05	0.000418	0.005644	2.82E-05	0.000697	0.009407	5.65E-05	0.001395	0.018815
Xiao and Martirossyan **[34]**	44.51758	1.44E+08	0.000135	0.024864	0.0029	0.000225	0.04144	0.004834	0.000449	0.082881	0.009667

* X (mm): Lateral displacement, M (N.mm): Moment, $\emptyset_{ultimate}$: Ultimate curvature, ε_s: Strain in tensile steel reinforcement. ε_s': Strain in compressive steel reinforcement.

Final displacement based on ASFI and MCFT methods

This study proposes the ASFI for both shear and flexure analysis which is based on the axial-shear-flexure Interaction effects. In the present study, the flexural mechanism is calculated by conventional analysis techniques, and the shear behaviour is modelled by the MCFT. Performing MCFT as a shear model in the ASFI method requires relatively intensive calculations which is conducted through the inverse of a 3×3 matrix and a convergence iteration process for five different variables. ASFI contains two methods, first one is based on a flexural model regarding conventional uniaxial analysis, and the second one considers a shear model based on a two-axis shear element method.

The bond-slip phenomenon is not explicitly accounted for in the analytical model when determining lateral displacement. The model primarily focuses on the interaction between axial, shear, and flexural responses to predict the overall displacement behaviour. Although bond-slip effects can influence the overall deformation capacity of reinforced concrete columns, these effects were not directly incorporated into the ASFI and MCFT framework presented here. Future refinements could consider the inclusion of bond-slip modelling to improve the accuracy of lateral displacement predictions, particularly in cases where reinforcement slip significantly contributes to deformation.

The entire lateral displacement of a column (γ) is the sum of shear (γ_s) and flexural displacements (γ_f). In addition, the total strain of the column (ε) is the sum up of the axial (ε_{xa}), shear (ε_{xs}) and flexural strain (ε_{xf}). On the other hand, axial strain of centre gravity (x_{cs}) is obtained from cross-sectional analysis with flexural-axial model and from the shear model for axial-shear elements the sum of shear and axial strains is calculated. Figure 2 portrait the above-mentioned calculations which lead to identifying axial stress in axial-flexural mechanism (σ_{xf}) and axial-shear mechanism (σ_{xs}). It is noteworthy that stresses in the axis perpendicular to the axis of the column (σ_y, σ_z) are ignored.

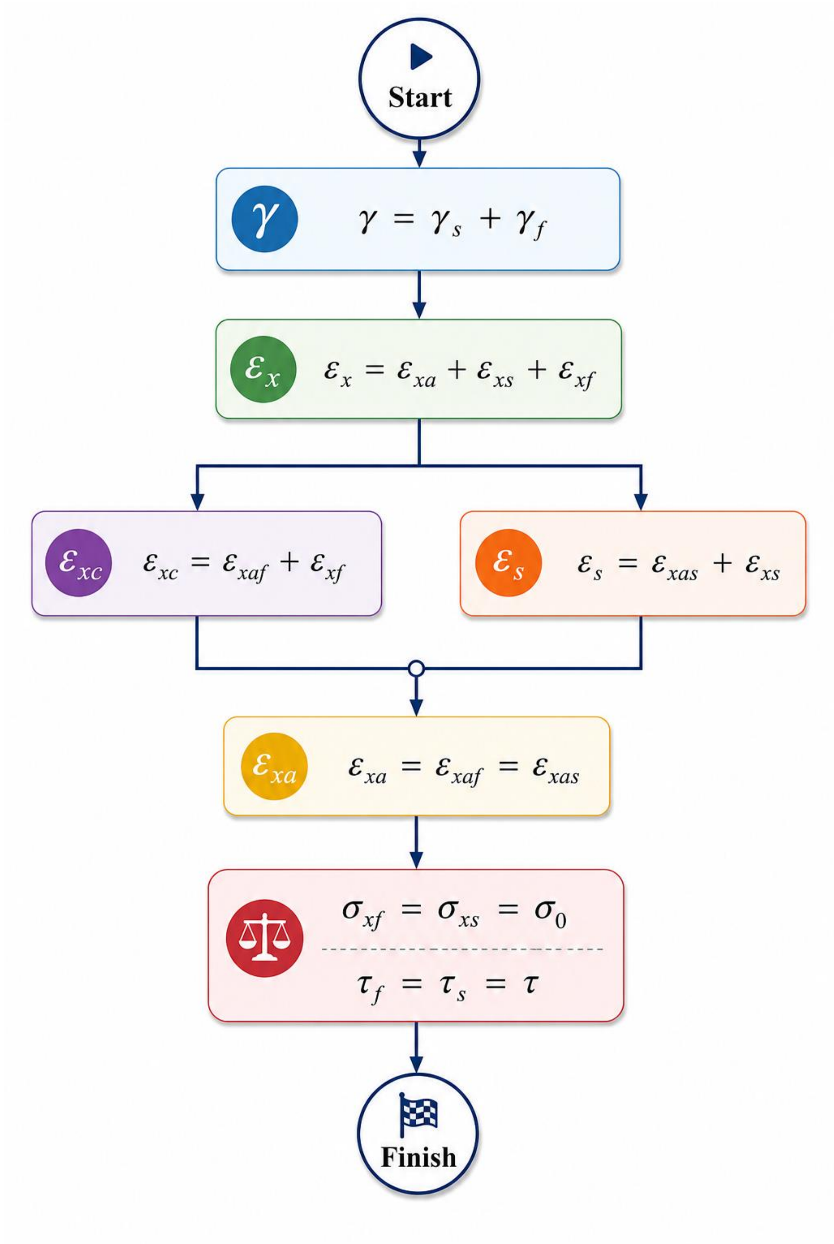

Figure 2. Flowchart for identifying equilibrium of axial and shear stresses of the flexural-axial model

To provide a broader perspective, Figure 3 illustrates two models: one for the shear-axial interaction and the other for the flexural-axial interaction, along with their coupling using spring sets. Additionally, Figure 4 presents the ASFI method applied to a reinforced concrete column with two end sections. Figure 5 shows the main compressive strain in a medium-height reinforced concrete column, which is fixed at the bottom and free at the top, subjected to both lateral and axial loads.

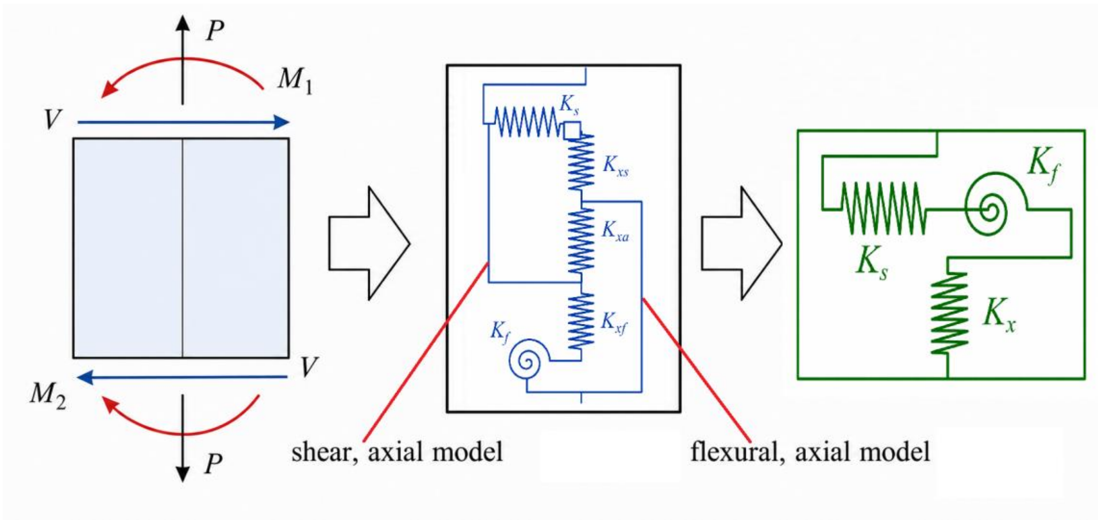

Figure 3. Spring model in ASFI method for both shear-axial and flexural-axial models

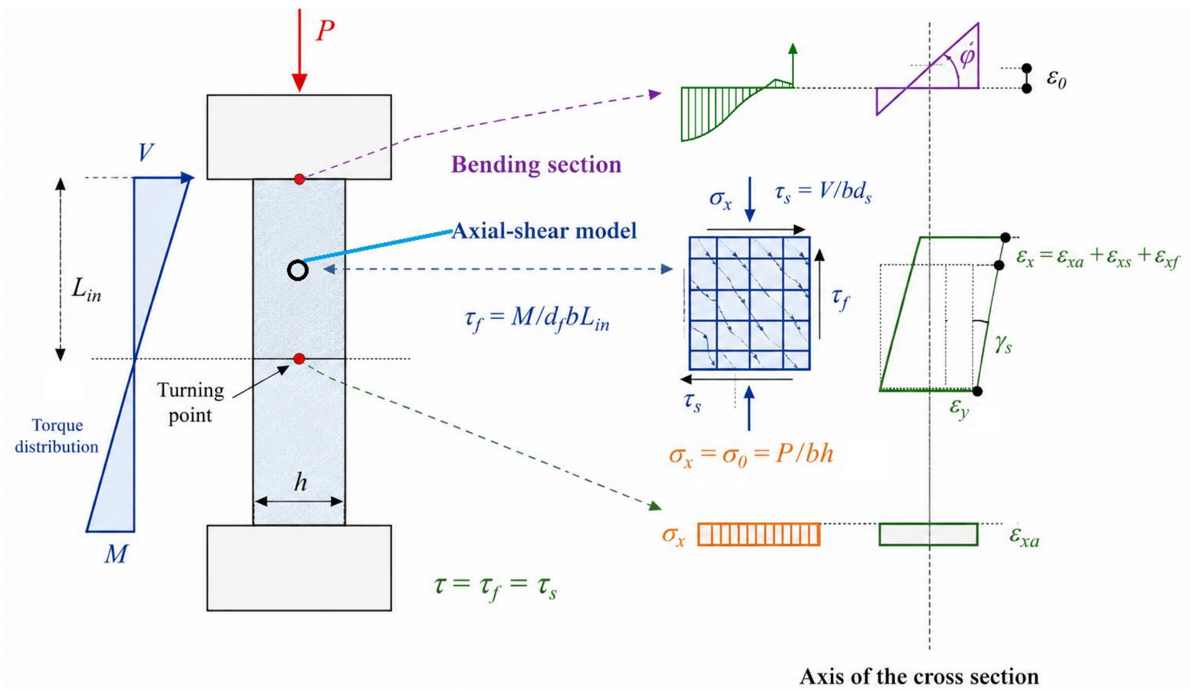

Figure 4. Interaction of flexural-shear-axial in ASFI method

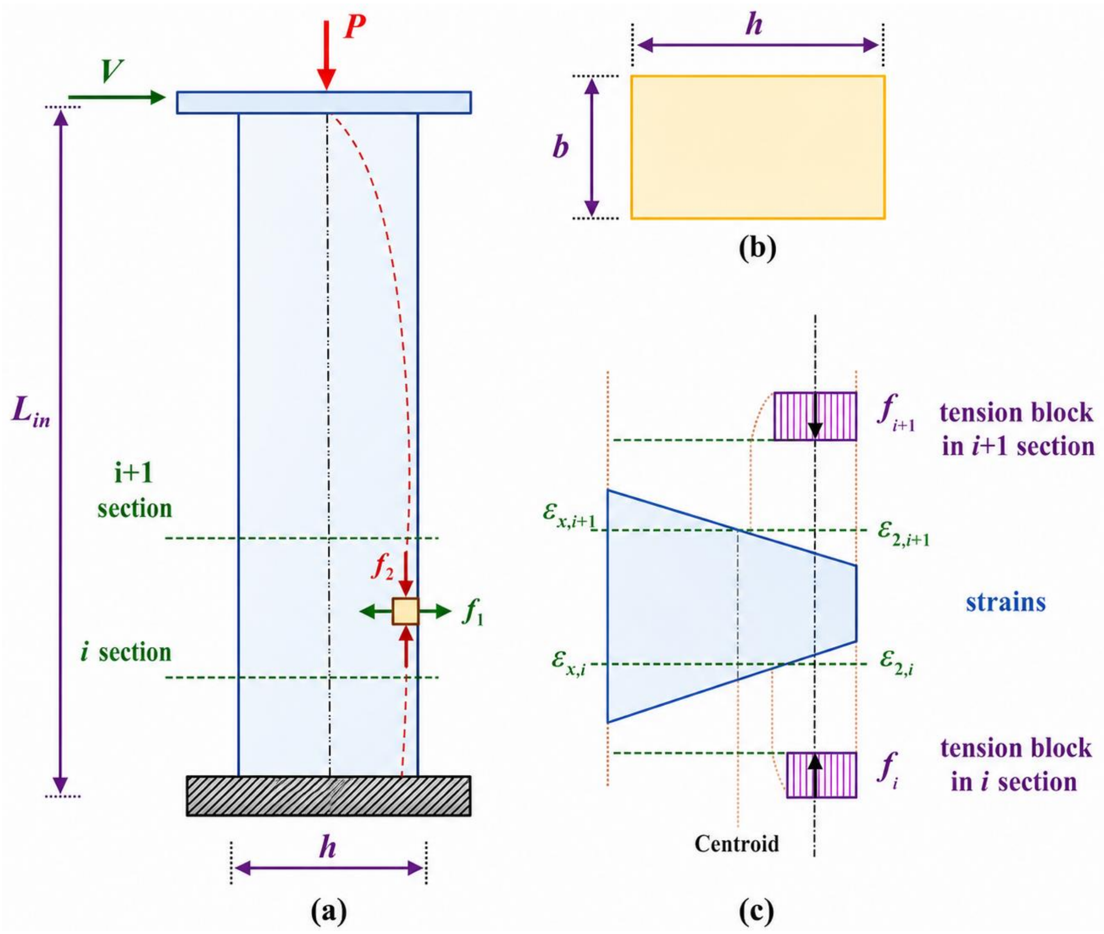

Figure 5. A reinforced concrete under axial-shear load, (a) principal stresses (f_1 and f_2), (b) section, (c) tension and strain in two adjacent sections

MCFT is a rotating crack model which considers compression softening effects and tension stiffening effects. In the calculation process of critical areas (fractures area), two points must be included, first, tensile shall be spread all over the concrete uniformly and second, shear stress should not exceed maximum shear strength of grains. Figure 6 depicted a reinforced concrete element in the MCFT framework.

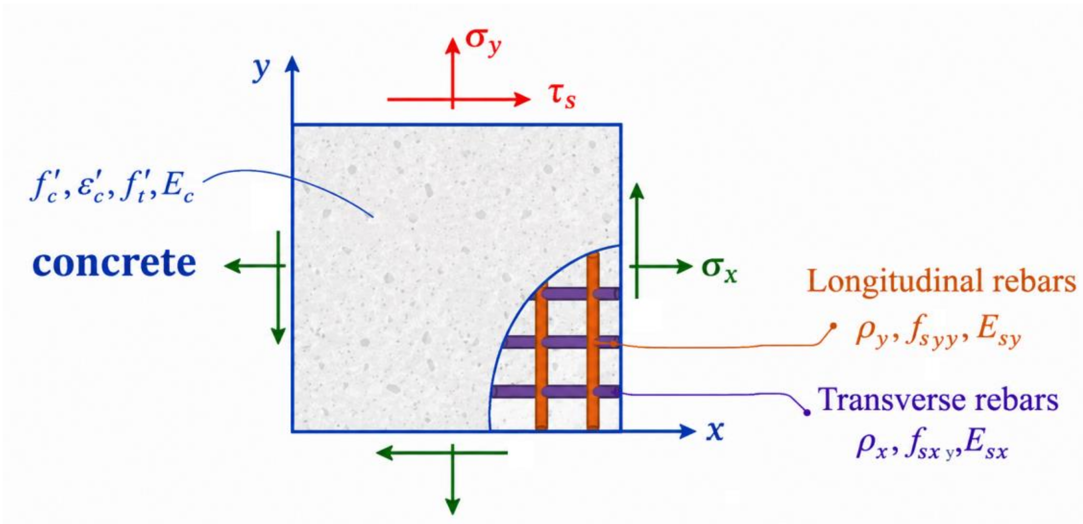

Figure 6. A reinforced concrete membrane element under flat stress, adopted from [35]

Additionally, in modelling the global shear behaviour, the ascending stage is captured using the MCFT to determine the initial shear strength. For the descending stage, the post-peak shear behaviour is modelled by incorporating a degrading shear stiffness in the shear spring element of the ASFI model. This degradation follows a bilinear or trilinear curve that simulates the reduction in shear capacity due to concrete cracking and aggregate interlock loss. Mathematically, the post-peak shear force ($Vpost$) can be represented as Eq. (3):

$$V_{post}=V_{peak}(1-\Delta_\gamma/\gamma_c) \tag{3}$$

where V_{peak} is the peak shear force, $\Delta\gamma$ is the incremental shear deformation, and γc is a characteristic shear deformation associated with ultimate capacity. This formulation ensures a gradual reduction of shear capacity beyond the peak, simulating the observed degradation in experimental tests.

Final deformation estimation process

Reinforcement failure, buckling of compression bars, rupture of tensile reinforcement, and concrete crushing are among the possible failure criteria in reinforced concrete members. In this study, however, shear failure is considered the governing failure mode, while the other mechanisms are also checked within the analytical procedure. The point of failure is defined as the stage in the iterative ASFI-MCFT procedure at which the governing stress-strain state reaches the limiting criterion of the controlling failure mode. Accordingly, failure is not identified solely from the visual peak of the lateral force-displacement curve, but from satisfaction of the MCFT-based failure condition in principal stress space. The final displacement and lateral load capacity are therefore taken at the onset of the governing failure mode. Three failure conditions are present by MCFT method including:

- Shear failure in a crack (mode 1)
- Failure due to loss of compressive strength (mode 2)

- Shear-compressive failure (mode 3)

Shear failure generally occurs because of lack in transverse rebar in column, and if the column categorized as a short reinforced concrete column the failure consider mode 2. Finally, when the columns are designed flexural with ductile performance, lack of transverse rebar and shear stress capacity, results mode 3 failure. Figure 7 illustrates formulas for each failure mode. It should be noted that the failure modes described in Figure 7 are intended as a conceptual representation based on observed shear behaviour. However, within the MCFT framework, calculations are performed in the principal stress space, where explicit cracking is not defined in the same manner. MCFT relies on evaluating the principal stresses to assess element failure. Therefore, while the failure modes are depicted in terms of shear stress for practical interpretability, the underlying analysis using MCFT is based on the principal stresses without directly defining cracks. Furthermore, the collapse location is identified as the critical section along the column where the governing ASFI-MCFT failure criterion is first satisfied during the iterative procedure. Therefore, collapse is determined analytically from the local stress-strain state and the controlling failure mode, rather than from a visual interpretation of the lateral force-displacement curve.

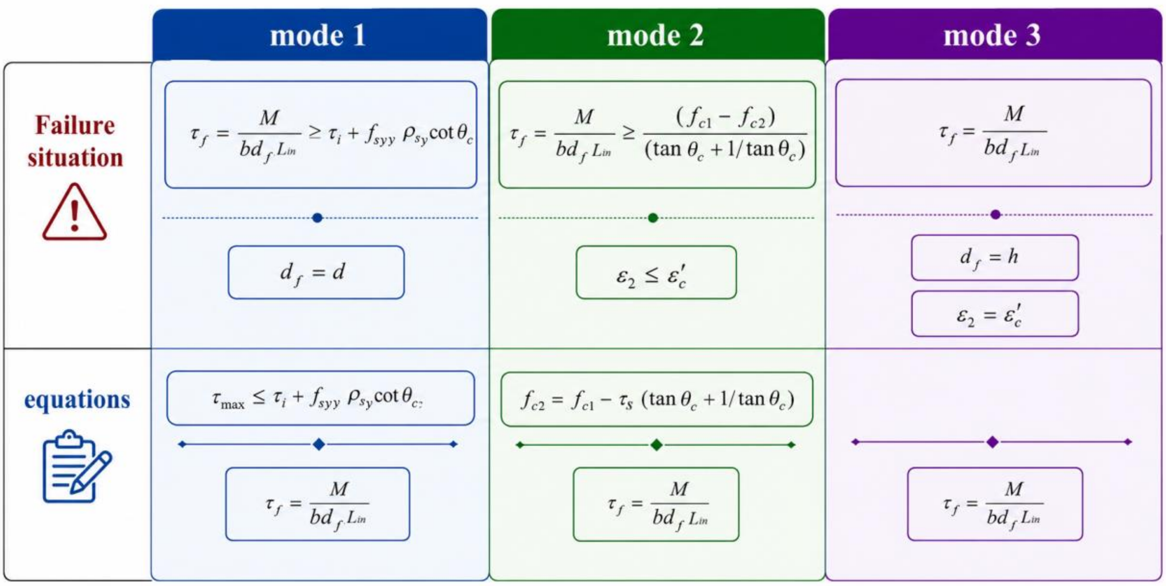

Figure 7. Three failure modes in the present study, their corresponding situations and equations

Final solution method

To solve the problem of analytical determination of the final displacement of reinforced concrete columns, the following process which is illustrated by Figure 8 is implemented in the Mathematica program. As it showed, first step is the assuming an initial value for compressive strain of concrete (ε_c) and after that, strain of cross section (ε_0) is calculated. The third step is determining the axial strain at the turning point with zero anchor (ε_{xa}). In this step, mean of modulus of elasticity of concrete section at turning point ($2\,f_p/\varepsilon_p$), strain (ε_p) and peak stress of enclosed concrete (f_p) are utilized. Next stage is calculating average main compressive and axial strain of concrete ($\varepsilon_2, \varepsilon_x$). After that, the main tensile strain of concrete (ε_1), Strain in transverse reinforcements (ε_y) and $tan^2\theta_c$are calculated. Controlling shear failure is the next step and after that, final displacement ratio which is also depicted in Figure 8 is calculated. Furthermore, a step-by-step example has been presented in the SI 2. Finally, lateral load capacity is obtained (v_u). Figure 9 illustrates the assumed curvature distribution for reinforced concrete columns before and after the tensile rebar flow.

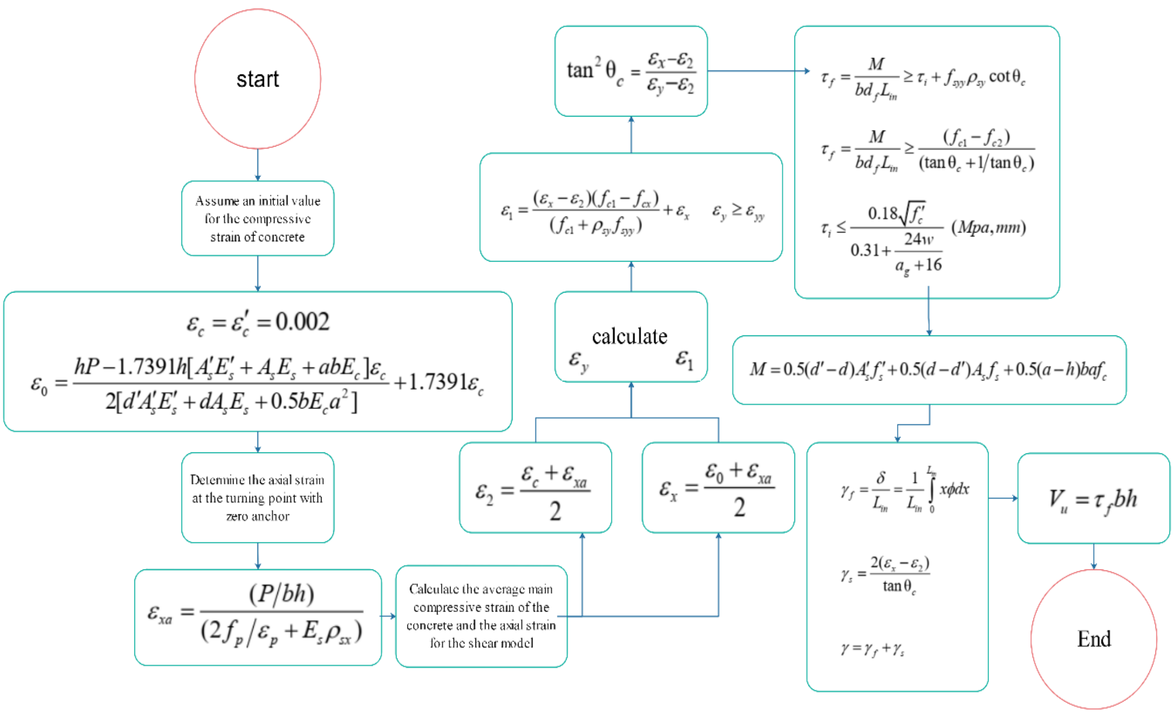

Figure 8. Steps for calculating final lateral load capacity in the present study

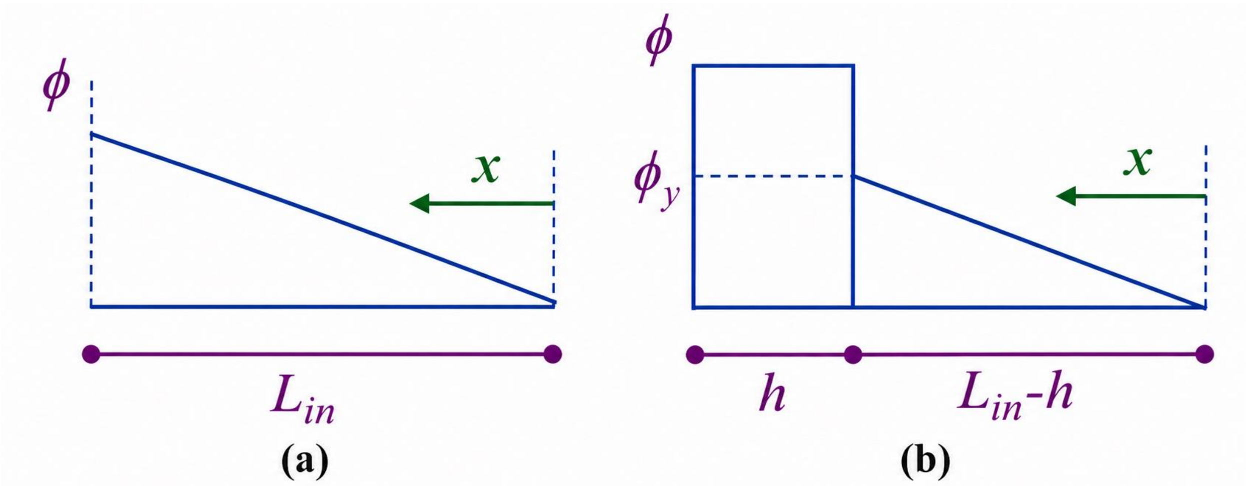

Figure 9. Assumed curvature distribution for reinforced concrete columns, (a) Before the tensile rebar flow (b) after the tensile rebar flow

The transformation of strain into lateral displacement is based on integrating the curvature derived from strain, consistent with the distribution shown in Figure 9. Mathematically, the lateral displacement (Δ) can be obtained by integrating the curvature (ϕ(x)) along the length of the plastic hinge as given in Eq. (4):

$$\Delta = \int 0 L \phi(x) dx \quad (4)$$

where L is the length of the plastic hinge. This integral accounts for the curvature over the column height, especially in the plastic hinge region. The length of plastic hinge is based on an empirical model for estimating the plastic hinge length [27] as Eq. 5.

$$\frac{l_p}{h} = \left[0.3\left(\frac{P}{P_0}\right) + 3\left(\frac{A_s}{A_g}\right) - 0.1\right]\left(\frac{L}{h}\right) + 0.25 \geq 0.25 \quad (5)$$

Where, lp is the plastic hinge length, h is the section depth of the column, P is the external axial load applied to the column, and P0 is the axial load capacity of the column. As is the total area of longitudinal reinforcing bars, Ag is the gross section area.

Furthermore, the proposed algorithm in Figure 8 does explicitly check the governing failure mode. The failure is identified through iteration by comparing stresses and strains against threshold values that indicate flexural, shear, or compression failure modes. Also, the effect of confinement (including its amount and geometric arrangement) on ductility and strain limits is incorporated by adjusting the ultimate compression limit of the concrete constitutive model. This is done by modifying the concrete's stress-strain curve, including the ultimate strain (ϵc), to reflect the increased capacity due to confinement. Spiral confinement generally leads to higher ultimate strain and better ductility compared to stirrup confinement, which is reflected in the constitutive relationships used.

Shear-Flexure Reliability Model

Sustainability is assessed through structural reliability: a column is sustainable if it reliably yields in flexure rather than failing in brittle shear, using efficient, not excessive, reinforcement. For each of the 11 specimens, nominal flexural capacity is computed from the idealized tension-compression steel couple (As, As', d, d', Table 1): Mn = As·fy·(d−d'). Following capacity-design logic [36], shear demand at flexural yielding is Vflex = Mn/L for the cantilever setup. Nominal shear capacity Vn = Vc+Vs follows ACI 318-style expressions [37] using section geometry, concrete strength, and tie detailing (Table 3). The limit state g = Vn − Vflex is propagated via a First-Order Second-Moment (FOSM) approach, using representative material coefficients of variation (COV_fc = 0.15, COV_fy = 0.05) consistent with the JCSS Probabilistic Model Code [38], giving reliability index β = mean(g)/std(g) and failure probability Pf = Φ(−β). Specimens with β ≥ 1.5 are classified flexure-governed, validated against the reported failure mode in Table 3. A second, aligned model, the Sustainability-Reliability Efficiency Index (SREI), normalizes β by steel mass invested per unit column volume, identifying specimens achieving reliable, ductile behaviour with least material. Both models share the same dataset, keeping results consistent across dashboards. All computations and dashboards were implemented in MATLAB R2019b, complementing rather than replacing the ASFI-MCFT predictions.

RESULTS AND DISCUSSION

In this part the results of the examination of 11 selected samples are presented. A subset of laboratory results on reinforced concrete columns that met the following conditions have been selected; The columns are considered with bending and bending-shear failure modes. Only columns with complete information have been used. Only the columns have been considered with the standard test process. Only the columns whose lateral resistance drop was recorded in the test were selected.

The main parameters that are used in the modelling and are effective on the final displacement of the columns are; Axial load index, Index related to confinement, Index of shear reinforcements, Compressive strength of concrete, Thinning and buckling of compression bars. It is assumed that the columns have appropriate operational details for acceptable seismic behaviour and the destruction of the column is done by bending. The lateral deformation of reinforced concrete columns under the effect of lateral loads consists of three parts: bending deformation, deformation caused by reinforcement sliding and shear deformation.

The experimental results are presented in this part. These results include the stress-strain curve output of core concrete, cover concrete and steel of each sample. Lateral-displacement-lateral force curve has been placed using the Mathematica software output and the theory of the displacement component model, which was the main goal of this research, and compared with the experimental results of the sample (Table 3). This curve is presented for the first sample in Figure 10 and the rest are demonstrated in the Appendix section. At the end, the failure mode of the samples is presented in Table 4.

Table 3. The specification of samples

			Section			Specifications of longitudinal rebars						Specifications of transverse rebars					
Samples	F'c (Mpa)	P(KN)	B(mm)	H(mm)	L(mm)	Rebar Diameter	Rebar Number	Ratio	Fy (Mpa)	Fu (Mpa)	Cover	Rebar Diameter	Tie distance	Ratio	Fy (Mpa)	Fu (Mpa)	Schematic
Soesianawati et al. [30], No. 1	46.5	744	400	400	1600	16	12	0.0151	446	702	13	7	85	0.0086	364	521	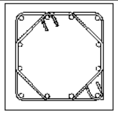
Soesianawati et al. [30], No. 2	44	2112	400	400	1600	16	12	0.0151	446	702	13	8	78	0.0122	360	492	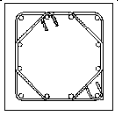
Soesianawati et al. (1986), No. 3	44	2112	400	400	1600	16	12	0.0151	446	702	13	7	91	0.008	364	521	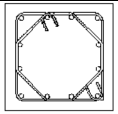
Soesianawati et al. [30], No. 4	40	1920	400	400	1600	16	12	0.0151	446	702	13	6	94	0.0057	255	402	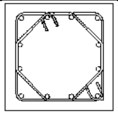
Zahn et al. [31], No. 5	28.3	1010	400	400	1600	16	12	0.0151	440	674	13	10	117	0.0156	466	688	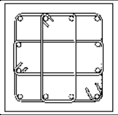
Zahn et al. [31], No. 6	40.1	2502	400	400	1600	16	12	0.0151	440	674	13	10	72	0.0199	466	688	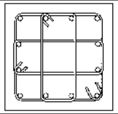
Tanaka and Park [32], No.7	25.6	819	400	400	1600	20	8	0.0151	474	721	40	12	80	0.0255	333	481	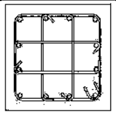

Watson et al. [33], No.8	40	3200	400	400	1600	16	12	0.0151	474	633.3	13	16	96	0.0032	388	518	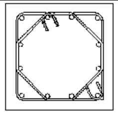
Watson et al. [33], No.9	42	4704	400	400	1600	16	12	0.0151	474	633.3	13	12	96	0.0126	308	444	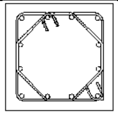
Watson et al., [33], No.10	38	4368	400	400	1600	16	12	0.0151	474	633.3	13	8	77	0.007	372	516	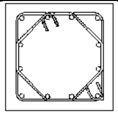
Xiao and Martirossyan [34], HC4-8L19-T10-0.1P	76	489	254	254	508	20	8	0.0355	510	675	13	10	51	0.0367	510	675	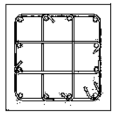

Table 4. The calculated parameters of the sample specifications

Sample	Failure mode	$\frac{s}{d_b}$	$\frac{\alpha\rho f_y}{f_c}$	$\frac{f_{le}}{(\alpha\rho f_y)}$	f_{cc}	f_c	$\frac{V_p}{V_n}$	l_p	$\frac{A_s}{A_g}$	$\frac{L}{h}$	$\frac{P}{P_0}$
Soesianawati et al. [30], No. 1	Bend	5.3	0.036	1.7	57.2	46.5	0.66	100	0.0151	4	0.1
Soesianawati et al. [30], No. 2	Bend-shear	4.9	0.057	2.5	59.5	44	0.80	156.5	0.0151	4	0.3
Soesianawati et al. [30], No. 3	Bend-shear	5.7	0.042	1.85	55.5	44	0.78	156.5	0.0151	4	0.3
Soesianawati et al. [30], No. 4	Bend-shear	5.9	0.026	1.05	46.94	40	0.92	156.5	0.0151	4	0.3
Zahn et al. [31], No. 7	Bend	7.3	0.138	3.9	49.3	28.3	0.59	172	0.0151	4	0.22
Zahn et al. [31], No. 8	Bend-shear	4.5	0.129	5.16	68	40.1	0.82	172.5	0.0151	4	0.39
Tanaka and Park [32], No.2	Bend	4	0.22	5.55	52	25.6	0.45	172	0.0151	4	0.2
Watson et al. [33], No.6	Bend	6	0.024	0.95	46	40	0.46	172.8	0.0151	4	0.5
Watson et al. [33], No.7	Bend	6	0.042	1.75	53	42	0.63	304	0.0151	4	0.7
Watson et al. [33], No.8	Bend	6	0.037	1.4	47	38	0.7	311.7	0.0151	4	0.72
Xiao and Martirossyan [34], HC4-8L19-T10-0.1P	Bend-shear	2.5	0.126	9.6	128	76	0.73	72.9	0.0355	2	0.04

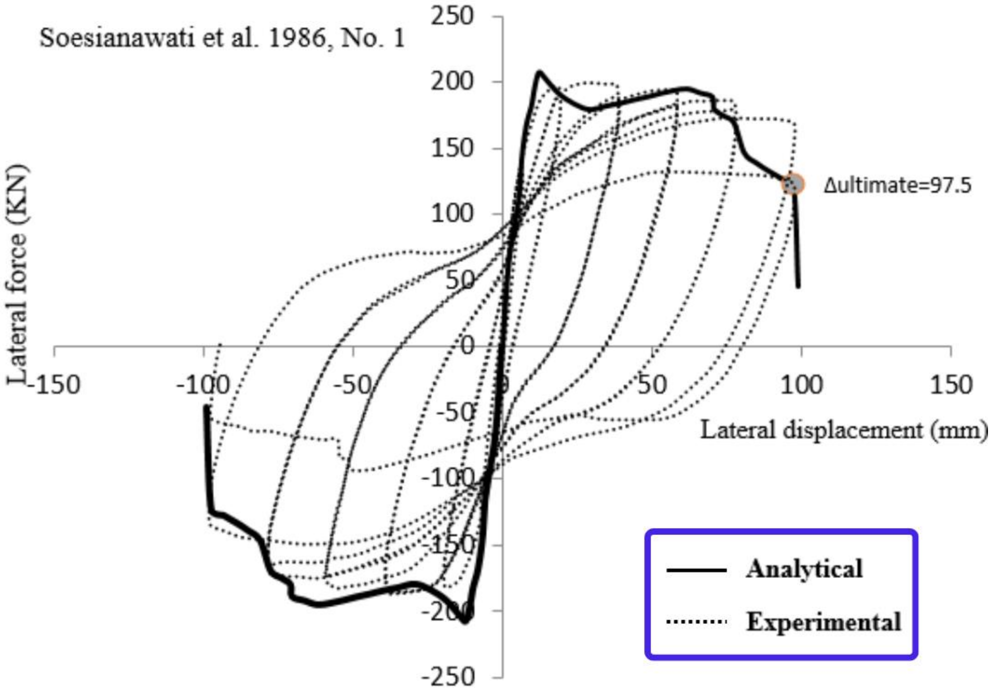

Figure 10. Lateral force-displacement curve resulted from Mathematica modelling and analysis

Figure 11 provides a quantitative statistical validation of the proposed ASFI–MCFT model against the experimental results for Specimen No. 1 [30], complementing the qualitative force-displacement comparison presented in Figure 10. Figure 11(a) compares the backbone (envelope) curves extracted from the experimental hysteresis loops and from the analytical prediction. The shaded region between the two curves marks the local force discrepancy, which stays small over most of the displacement range but widens beyond approximately ±75 mm, consistent with the post-yield deviation discussed in the main text. Figure 11(b) presents a parity plot of predicted versus observed force built from matched points; the fitted regression (slope = 0.99, intercept = −7.6 kN) lies close to the 1:1 reference line, and the coefficient of determination (R^2 = 0.99) confirms a strong linear correspondence between analytical and experimental forces across both loading branches. Figure 11(c) summarizes the percentage difference between the analytical model and the experimental test for five key response parameters: initial stiffness, peak force in the positive and negative directions, and displacement capacity in both directions. The model overestimates initial stiffness by 10.9% and the positive peak force by 2.8%, while underestimating the negative peak force by 8.4%; displacement capacity is captured almost exactly in both directions (+1.6% and +0.0%). Together, Figure 11(a–c) shows that the ASFI–MCFT model reproduces the overall force-displacement envelope with good accuracy

(RMSE = 17.4 kN, MAE = 13.1 kN, MAPE = 8.0%), while confirming the asymmetric strength bias in the negative loading direction noted qualitatively in Figure 10.

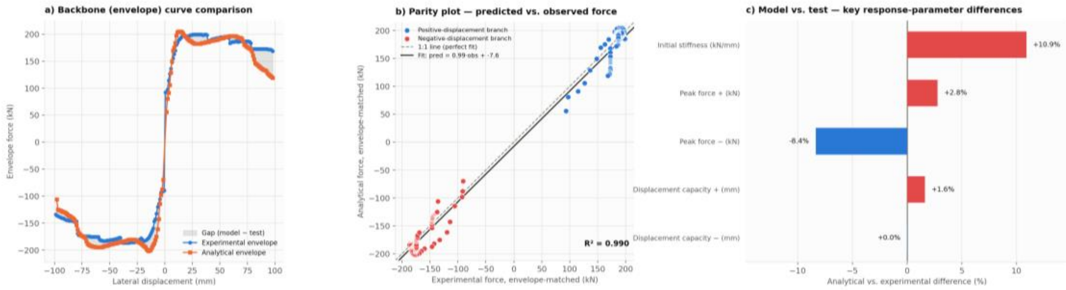

Figure 11. Statistical validation of the ASFI–MCFT model against test data (Specimen No.1): (a) envelope comparison, (b) parity plot ($R^2 = 0.99$), (c) percentage differences in stiffness, peak force, and displacement capacity.

Figure 12 summarizes the key mechanical and geometric parameters of the eleven column specimens used to validate the analytical model, distinguishing between bend-critical (blue) and bend-shear-critical (red) failure modes throughout.

Figure 12(a) presents the axial load ratio (P/P_0) for each specimen. Values range from as low as 0.04 [34] to as high as 0.73 (Watson et al. [33] No. 10), with the Soesianawati et al. [30] and Zahn et al. [31] specimens clustering in the 0.2–0.4 range. Notably, both very low and very high axial load ratios appear across both failure-mode categories, suggesting that axial load ratio alone does not cleanly separate bend from bend-shear behaviour in this dataset.

Figure 12(b) examines the relationship between tie spacing normalized by bar diameter (s/d_β) and shear demand ratio (V_p/V_n). The near-zero correlation (r = −0.09) and the flat linear fit indicate that confinement spacing has little systematic influence on shear demand across the specimens, though bend-shear specimens (triangles) tend to occupy the higher shear-demand region (0.75–0.95) at moderate tie spacing, while bend specimens (circles) are more scattered, including at wider tie spacing (>7).

Figure 12(c) shows a much stronger relationship (r = 0.88) between unconfined concrete strength (f′c) and confined strength (f_cc), with all points lying above the 1:1 line, confirming that confinement consistently enhances strength beyond the base concrete capacity. The linear fit diverges further from the 1:1 line as f′c increases, indicating that confinement effects become more pronounced at higher unconfined strengths, most dramatically illustrated by the bend-shear specimen near f′c = 75 MPa reaching f_cc ≈ 128 MPa.

Figure 12(d) consolidates these relationships into a correlation matrix across five parameters. The strongest correlations are the perfect negative relationship between L/h and A_s/A_o (r = −1.00) and the strong positive relationship between s/d_β and L/h (r = 0.72), reflecting geometric interdependencies among specimen slenderness, reinforcement ratio, and confinement spacing. In contrast, V_p/V_n shows weak correlations with all other parameters ($|r| \leq 0.10$), reinforcing the Figure 12(b) finding that shear demand behaves largely independently of the geometric and axial-load parameters examined.

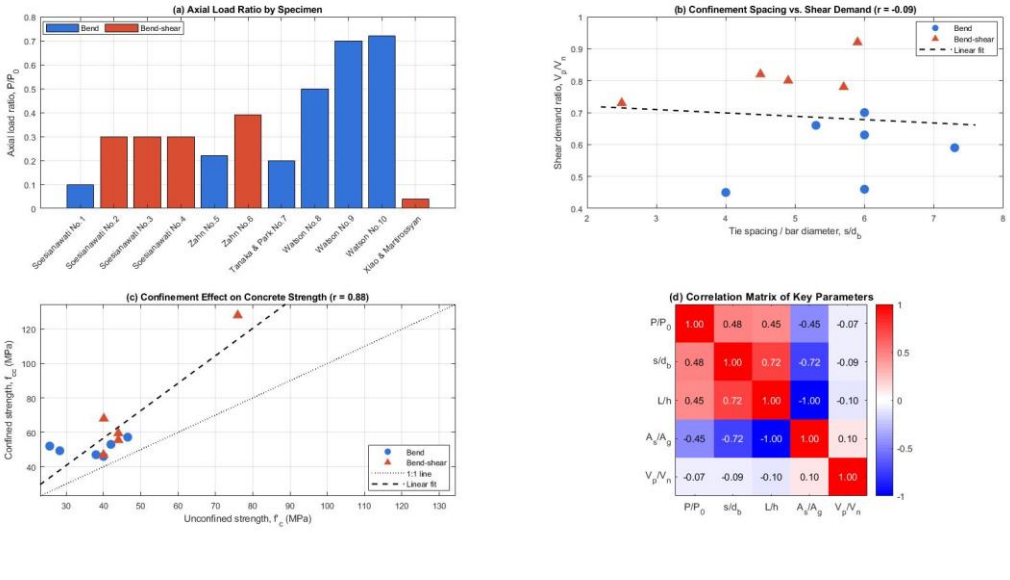

Figure 12. Specimen dataset overview: (a) axial load ratio by specimen; (b) tie spacing vs. shear demand; (c) confinement effect on concrete strength; (d) correlation matrix of key parameters. Bend vs. bend-shear specimens shown in blue/red.

Figure 13 evaluates the analytical model's predictive accuracy in two complementary ways: a specimen-level error breakdown on the left and a study-wide statistical summary on the right.

The left panel presents a bar chart of the percentage difference (analytical minus experimental) for Specimen No. 1 [30] across four response quantities. Initial stiffness shows the largest positive deviation, with the model overestimating by roughly 11%. Peak force in the positive loading direction is well captured, with a modest overestimate of about 3%, while peak force in the negative direction shows the model underestimating capacity by approximately 8%, the largest discrepancy in the chart. Displacement capacity in the positive direction is predicted closely, with only a slight overestimate near 1.5%, whereas no bar appears for displacement capacity in the negative direction, indicating either a negligible difference or that this value was not distinctly reported for this specimen.

The right panel complements this specimen-specific view with quantitative goodness-of-fit statistics for Specimen No. 1 based on Figure 11: an RMSE of 17.4 kN, MAE of 13.1 kN, and MAPE of 8.0%, alongside a regression fit of $R^2 = 0.99$ with a slope of 0.99 and an intercept of −7.6 kN — indicating a near-ideal linear correspondence between analytical and experimental force values for this specimen. The panel then situates this single-specimen result within the broader, qualitative conclusions drawn across all eleven specimens: initial stiffness and yield displacement show good agreement overall, but the model systematically overestimates post-yield ductility, particularly for bend-shear (shear-critical) specimens.

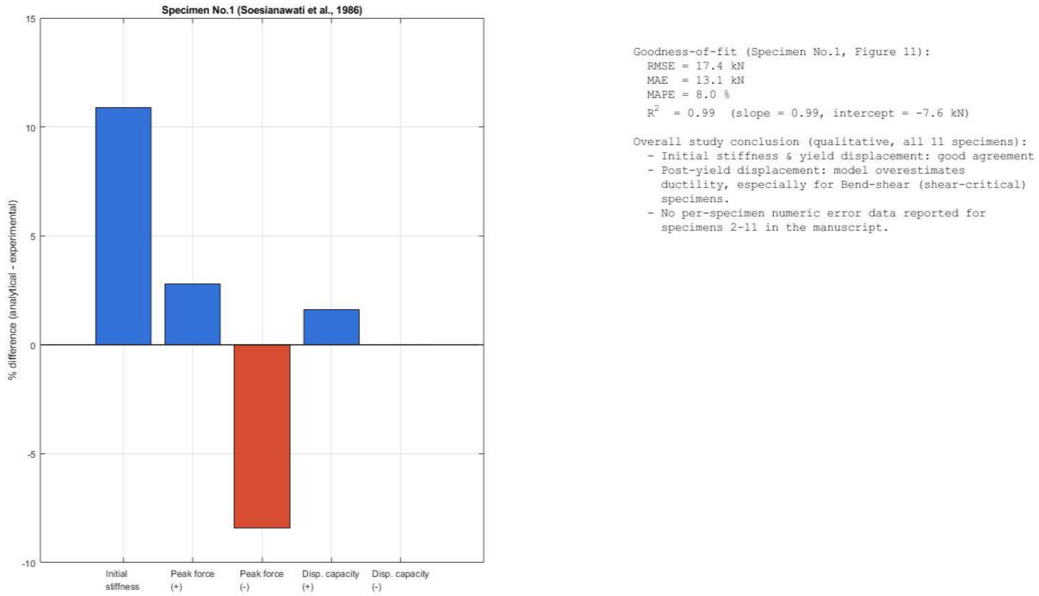

Figure 13. Model accuracy assessment: percentage differences in stiffness, force, and displacement for Specimen No.1, alongside goodness-of-fit statistics and qualitative conclusions across all 11 specimens, highlighting post-yield ductility overestimation.

Figure 14 presents the four-panel output of the shear-flexure reliability assessment applied to the eleven validated column specimens. Figure 14(a) shows the reliability index β computed for each specimen, ranging from roughly 7.3 for Soesianawati et al. [30] No. 4, the least reliable case, up to 19.3 for Watson et al. [33] No. 8, with every specimen sitting well above the target threshold of $\beta = 1.5$. This indicates that, under the first-order second-moment formulation, the nominal shear capacity of each column comfortably exceeds the shear demand generated at the point of flexural yielding, so ductile flexural behaviour is the reliably expected outcome rather than an occasional or marginal one. Figure 14(b) translates these reliability indices into probabilities of brittle shear failure, and the values are effectively zero across the dataset, on the order of 10^{-13} or smaller. The one visible exception is Soesianawati et al. [30] No. 4, which shows a small but non-zero spike consistent with its comparatively lower β in Figure 14(a); it is the specimen with the weakest reliability margin, even though that margin remains large in absolute terms.

Figure 14(c) reinforces this picture geometrically by plotting nominal shear capacity against the shear demand corresponding to flexural yielding for each specimen. Every data point falls above the diagonal line representing equal capacity and demand, confirming that flexural yielding governs the response in all eleven cases rather than shear. The color scale, keyed to β, shows that the specimens with the largest reliability margins also sit farthest above this line, giving a continuous rather than binary sense of how much safety margin each design carries. Figure 14(d) closes the loop by checking these reliability-based classifications against the actual experimental failure modes reported in Table 3. Nine of the eleven specimens show agreement between the predicted, flexure-governed classification and the reported mode, while Soesianawati et al. [30] No. 3 and No. 4 stand out as mismatches. That discrepancy is worth stating plainly in the paper rather than smoothing over, since it points to a real limitation of the simplified capacity formulation in representing shear vulnerability for those two specimens, and it is exactly the kind of honest boundary case that strengthens rather than undermines the credibility of the reliability framework.

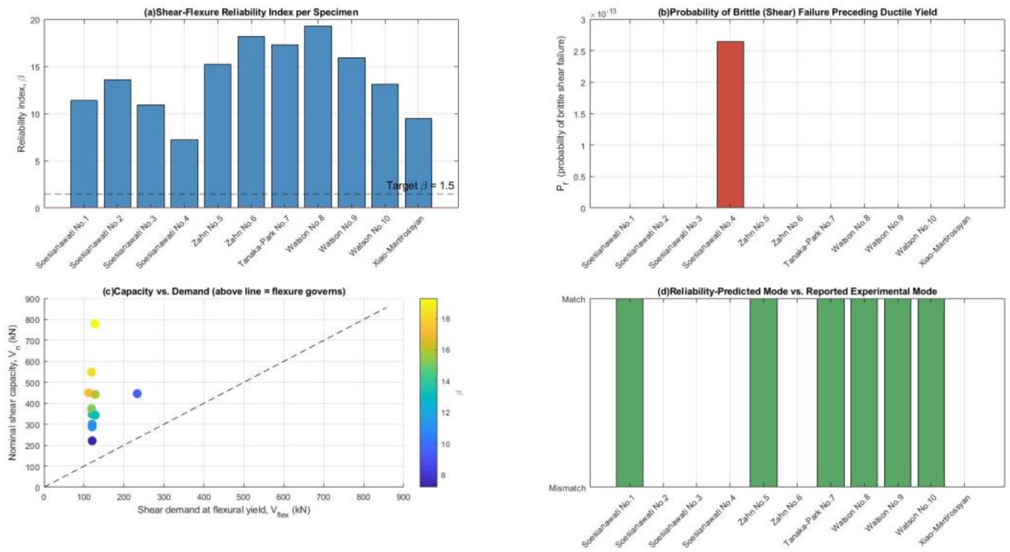

Figure 14. Shear-flexure reliability of the 11 specimens: (a) reliability index β, (b) brittle-failure probability, (c) capacity vs. demand margin, (d) predicted vs. reported mode.

Figure 15 presents the Sustainability-Reliability Efficiency Index (SREI) results and read together with Figure 14 it shows that reliability and material investment are not the same thing. Figure 15(a) ranks the eleven specimens by SREI, the reliability achieved per unit of steel invested, and the ordering is striking: Soesianawati et al. [30] No. 3 and No. 1 top the list with the highest efficiency, while Xiao-Martirossyan [34] sits near the bottom and Soesianawati et al. [30] No. 4 registers essentially zero. This is a direct continuation of the mismatch flagged in Figure 14, where Soesianawati et al. [30] No. 3 and No. 4 were the two specimens whose predicted failure mode disagreed with the reported one; here they land at opposite ends of the efficiency ranking, which suggests the disagreement in Figure 14 is not a uniform modelling error but reflects genuinely different reinforcement-to-reliability trade-offs between the two specimens.

Figure 15(b) makes the underlying reason visible by plotting reliability index β against steel invested per cubic meter of column, coloured by the transverse confinement ratio. Most specimens cluster in a modest steel range of roughly 140 to 220 kg/m³ while still achieving β values between 7 and 19, but Xiao-Martirossyan [34] is a clear outlier, using nearly 475 kg/m³ of steel, more than double any other specimen, yet reaching only a middling β of about 9.5. Watson et al. [33] No. 8, by contrast, achieves the highest reliability in the entire dataset, β ≈ 19.3, with a comparatively modest steel investment and a low confinement ratio. Figure 15(c) checks whether axial load utilization explains this pattern and finds only a weak, noisy upward trend between the axial load ratio and β, indicating that how heavily a column is loaded relative to its axial capacity is a secondary factor; the confinement and reinforcement detailing captured in Figures 15 (a) and (b) matter more. Figure 15(d) closes the figure by placing steel invested and rescaled β side by side for every specimen, and the same story repeats visually: Xiao-Martirossyan's [34] steel bar dwarfs every other specimen's, but its reliability bar is one of the shorter ones in the set, while Watson et al. [33] No. 8 reaches the tallest reliability bar without a correspondingly large material bar. Taken together, the figure supports the core sustainability argument of the framework: reliable, ductile-governed seismic performance can be achieved without proportionally large reinforcement, and some of the heaviest-reinforced specimens in this dataset are, in fact, the least efficient at converting that material into reliability.

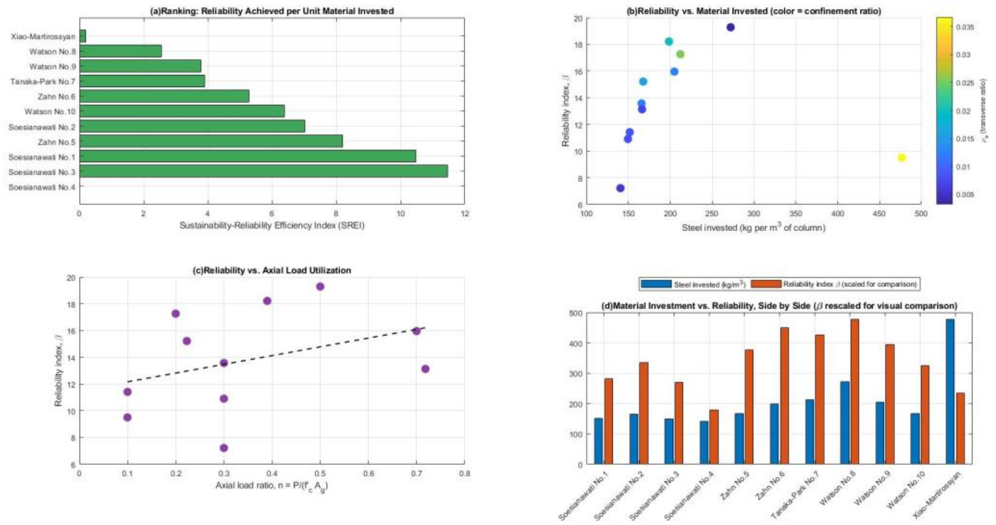

Figure 15. Sustainability-reliability efficiency of 11 specimens: (a) SREI ranking, (b) reliability vs. steel invested, (c) reliability vs. axial load ratio, (d) material vs. reliability comparison.

Comparing the experimental results to the analytical model predictions reveals some key insights. The validation results presented in this study indicate that while the ASFI and MCFT model captures the initial stiffness and yield displacement of reinforced concrete columns under lateral cyclic loading reasonably well, there is a significant discrepancy between the predicted and observed behaviour in the post-yield region. This discrepancy becomes increasingly pronounced as the columns undergo higher levels of inelastic deformation. The primary reasons for this include limitations in modelling shear stiffness degradation, rebar buckling, and concrete crushing effects, which are challenging to represent accurately using the current formulation. The existing model does not fully account for progressive deterioration mechanisms such as bond-slip effects, loss of aggregate interlock, and rebar buckling, which significantly influence the post-yield stiffness and ductility. These effects contribute to a reduction in lateral load capacity after yielding, leading to the observed differences in the force-displacement curves. To improve the accuracy of the prediction model, future work will focus on integrating more sophisticated material constitutive models that can better represent these deterioration processes. This will include incorporating bond-slip effects between reinforcement and concrete, a more refined representation of compression softening, and fracture mechanics for rebar and concrete. By enhancing these aspects, we expect to reduce the observed discrepancies and provide a more accurate prediction of the full hysteretic behaviour of reinforced concrete columns under seismic loading.

The findings indicate that the proposed analytical model effectively captures the general load-displacement behaviour and failure modes of the tested columns. The initial stiffness and yield points align closely with experimental observations across most samples, demonstrating the model's ability to accurately represent the elastic and early inelastic responses of reinforced concrete columns. However, discrepancies arise in the post-yield behaviour, where the model tends to overestimate displacement capacity, particularly in columns exhibiting shear failures. This suggests that the model's representation of shear mechanisms requires refinement to improve accuracy.

The observed differences may also stem from variations in material properties and geometric imperfections in the actual columns that are not fully captured by the analytical assumptions. While the model shows promise in predicting the seismic deformation capacity of RC columns, its validation is limited by the relatively small number of tested samples, which restricts its generalizability and robustness.

To address these limitations, future research should include validation against a more diverse dataset encompassing a broader range of column configurations, failure modes, and material properties. Additionally, conducting parametric studies could offer deeper insights into the model's sensitivity to key structural parameters, helping to identify areas for further improvement. Refining the model to better incorporate shear effects would enhance its predictive accuracy, particularly for shear-critical columns.

The experimental results also illustrate the progression of damage and failure modes in the tested columns. Initial flexural cracking occurs under small drifts around 0.5-1%. As drift increases to 1-2%, more extensive flexural cracking develops along with initiation of rebar yielding. At drifts of 2-4%, damage localizes in plastic hinge regions near column ends with concrete spalling and rebar buckling. Shear-critical columns experience inclined shear cracking in this stage as well. Ductile flexural failures occur after 4% drift typically, involving fracture of previously yielded rebars. For shear-critical columns, brittle diagonal shear failures happen earlier around 1-2% drift when crack widths exceed capacity of transverse reinforcement. These observed behaviours align with expectations from theory and past experiments. Comparing to analytical model predictions shows good agreement in initial elastic stiffness and yield displacement, verifying the model accurately captures the uncracked column and flexural cracking states. Differences arise in post-yield drifts over 2% as damage accumulates. The model overestimates displacement capacity of some columns, especially shear-critical ones, by not fully accounting for strength deterioration from rebar buckling, concrete crushing, and shear mechanisms.

Refinements to the analytical model could provide better accuracy in several areas. The fixed crack angle assumption in MCFT could be relaxed to allow shear cracking to localize more realistically. Enhanced material models to represent progressive concrete crushing and rebar buckling in compression would improve softening predictions. Fracture modelling of rebar and shear links could simulate loss of capacity from reinforcing failures. Accounting for residual crack widths would enable simulation of pinched hysteretic behaviour observed experimentally.

The lateral force-displacement behaviour and progression of damage for the reinforced concrete columns aligns with extensive experimental evidence from past seismic column testing. Tests by Aboutaha et al. [39] on high-strength concrete columns observed initial flexural cracking around 1-2% drift followed by rebar buckling and fracture leading to strength loss, similar to the failure sequence noted here. Sheikh and Yau [40] examined columns with varying tie-spacing, finding closely-spaced ties increased drift capacity up to 5%, while widely spaced ties led to premature shear failures below 1% drift akin to the shear-critical columns in this study. Prakash et al. [41] and Hadi [42] both conducted cyclic tests on columns confirming shear displacements contributed less than flexural displacements to total drift, further validating the ASFI/MCFT decomposition here. Research by Kahn and Mitchell [43] and Ozbakkaloglu and Saatcioglu [44] quantified the pinching and stiffness degradation in column hysteresis under increasing displacements, consistent with the experimental results.

On the analytical side, modelling by Guner and Vecchio [45] and Palermo and Vecchio [46] accurately captured post-peak softening by incorporating compression crushing and rebar buckling mechanisms that are simplified in the current model.

Read against the 2026 literature, the ASFI–MCFT study sits within a field that is visibly bifurcating into two complementary tracks: recalibrated mechanics-based models and data-driven surrogate models, and the manuscript would benefit from acknowledging both. Yılmaz [47] recalibrates the Disturbed Stress Field Model (DSFM), MCFT's direct descendant, for beam-column joints and shows that compression softening is "overwhelmingly governed by principal compressive strain," not the tensile-cracking measures panel theories usually assume; re-expressing softening as a power law of that single strain removed systematic conservatism, lifting the mean strength ratio from 0.85 to 1.01 and cutting the coefficient of variation from 34.5% to 13%. This is directly diagnostic for the present paper: Figure 11 reports the same signature of systematic bias (initial stiffness +10.9%, positive peak force +2.8%, negative peak force −8.4%), and an inverse-calibration exercise of this kind, rather than the currently fixed MCFT constitutive laws, could plausibly close much of that gap and should be flagged as concrete future work rather than a generic limitation.

The three machine-learning studies found [48–50] sharpen the paper's own stated limitation about its 11-specimen dataset. Sadeghi et al. trained ensemble models, XGBoost performing best, on 200 corroded-column tests to reproduce the full backbone including post-peak degradation, exactly the regime this paper's abstract admits the ASFI–MCFT model overestimates. Cui et al. [50], using 312 steel-reinforced concrete (SRC) column tests, showed R^2 gains of 26.5–32.9% over conventional formulas once sample size grew past the small-dataset regime this paper occupies. Mehta et al. [49] extended the same logic to failure-mode classification for joints. Together they suggest the present model's three MCFT failure modes could be repositioned as physics-informed features feeding a learned classifier once a larger multi-source specimen library is assembled, rather than treated as a standalone deterministic criterion; this would also mitigate the generalizability concern the authors already raise in the Conclusion. Xiao et al. [51] offers the closest methodological mirror: a theoretical shear-capacity model for engineered cementitious composite (ECC)-shell-strengthened joints validated against tests and simulation with 7.5% and 7.9% maximum deviation.

CONCLUSION

This study introduces a novel analytical approach utilizing ASFI and MCFT to predict the seismic response of reinforced concrete columns. The methodology's efficacy was confirmed through validation against experimental data from 11 columns subjected to cyclic lateral loading. While the model successfully mirrored initial stiffness, yield displacement, and failure modes, it revealed limitations in post-yield displacement prediction, particularly for shear-critical columns, where ductility was overestimated. To address these limitations, it is imperative to integrate localized shear cracking, progressive concrete and rebar buckling, and fracture modelling into the framework. This work represents a significant step toward developing validated analytical techniques for simulating the complex behaviour of reinforced concrete columns during earthquake events. However, to improve the robustness and reliability of the proposed methodology, further experimental validation and model refinement are essential. Expanding the verification dataset to encompass a broader spectrum of column configurations, failure modes, and experimental conditions is crucial for enhancing the model’s credibility and applicability. Such an expansion would increase the universality of the theoretical framework and enable more precise refinements to ensure accuracy across diverse structural scenarios. Additionally, incorporating advanced computational techniques and leveraging larger-scale experimental datasets could provide deeper insights into the intricate nonlinear behaviours of reinforced concrete columns under seismic loading, further advancing the methodology’s development and practical utility.

In conclusion, this research provides a robust analytical foundation with considerable potential for advancement, making it an asset in the realm of column seismic design and evaluation. Despite the successful demonstration of the ASFI and MCFT-based modeling approach, continued development is necessary to comprehensively capture observed strengths, ductility, and failure modes. Further efforts should focus on incorporating advanced localized shear cracking, comprehensive concrete and rebar buckling, and fracture modeling to augment the model's predictive capabilities. Additionally, expanding the dataset for a wider range of column configurations and prioritizing accuracy in post-yield drift predictions are vital for comprehensive validation and practical application.

CONFLICT OF INTERESTS

The authors confirm that there is no conflict of interest associated with this publication.

APPENDIX

Appendix is available in online supplement attached.

REFERENCES

1. Khanmohammadi M, Eshraghi M, Behboodi S, Mobarake AA, Nafisifard M. Dynamic characteristics and target displacement of damaged and retrofitted residential buildings using ambient vibration tests following Sarpol-e Zahab (Iran) Earthquake (MW 7.3). Journal of Earthquake Engineering. 2022;26(12):6015–6041.
2. Garshasbi M, Kabir G, Dutta S. Stormwater infrastructure resilience assessment against seismic hazard using Bayesian belief network. International Journal of Environmental Research and Public Health. 2023;20(16):6593.
3. Shakib H, Dardaei S, Farhangian H, Torkanbouri NE. Seismological Aspects and Seismic Behavior of Buildings During the M 7.3 Western Iran Earthquake in Sarpol-e-zahab Region. Iranian Journal of Science and Technology, Transactions of Civil Engineering. 2022;46(4):3063–3079. doi:10.1007/s40996-021-00737-1
4. Tunc TE, Tunc G. Transferring Technical Knowledge to Turkey: American Engineers, Scientific Experts, and the Erzincan Earthquake of 1939. Notes and Records: the Royal Society Journal of the History of Science. 2022;76(3):387–406. doi:10.1098/rsnr.2020.0054
5. Tshuma M, Belle JA, Ncube A, Nyam YS, Orimoloye IR. Building resilience to hazards in the water, sanitation, and hygiene (WASH) systems: a global review. International Journal of Environmental Health Research. 2024;34(1):466–478. doi:10.1080/09603123.2022.2153809

6. Hansu O, Güneyisi EM. Comparison of Novel Seismic Protection Devices to Attenuate the Earthquake Induced Energy. Actuators 2021, 10, 73. s Note: MDPI stays neutral with regard to jurisdictional claims in published …; 2021.
7. Samadian D, Ghafory-Ashtiany M, Naderpour H, Eghbali M. Seismic resilience evaluation based on vulnerability curves for existing and retrofitted typical RC school buildings. Soil Dynamics and Earthquake Engineering. 2019;127:105844. doi:10.1016/j.soildyn.2019.105844
8. Dębski W, Klejment P. Earthquake physics beyond the linear fracture mechanics: a discrete approach. Philosophical Transactions of the Royal Society A. 2021;379(2196):20200132.
9. Ghosh S, Ghosh S, Chakraborty S. Seismic fragility analysis in the probabilistic performance-based earthquake engineering framework: an overview. International Journal of Advances in Engineering Sciences and Applied Mathematics. 2021;13(1):122–135.
10. Peruš I, Poljanšek K, Fajfar P. Flexural deformation capacity of rectangular RC columns determined by the CAE method. Earthquake Engineering & Structural Dynamics. 2006;35(12):1453–1470. doi:10.1002/eqe.584
11. Tagle SJ, Jünemann R, Vásquez J, De La Llera JC, Baiguera M. Performance of a reinforced concrete wall building subjected to sequential earthquake and tsunami loading. Engineering Structures. 2021;238:111995. doi:10.1016/j.engstruct.2021.111995
12. Li L, Luo G, Wang Z, Zhang Y, Zhuge Y. Prediction of residual behaviour for post-earthquake damaged reinforced concrete column based on damage distribution model. Engineering Structures. 2021;234:111927.
13. Marder K, Elwood KJ, Motter CJ, Clifton GC. Post-earthquake assessment of moderately damaged reinforced concrete plastic hinges. Earthquake Spectra. 2020;36(1):299–321. doi:10.1177/8755293019878192
14. Zhou Y, Zheng S, Chen L, Long L, Wang B. Experimental investigation into the seismic behavior of squat reinforced concrete walls subjected to acid rain erosion. Journal of Building Engineering. 2021;44:102899. doi:10.1016/j.jobe.2021.102899

15. Hamoda A, Shahin RI, Ahmed M, Abadel AA, Ng AW, Liang QQ. Behavior of circular reinforced concrete columns strengthened with corrugated steel sheets and high-performance concrete. In: Structures. Vol. 70. Elsevier; 2024. p. 107938.
16. Erdem RT, Bağcı M, Demir A. A comparative evaluation of performance based analysis procedures according to 2007 Turkish Earthquake Code and FEMA-440. Mathematical and Computational Applications. 2011;16(3):605–616.
17. Daei A, Zarrin M. Assessing seismic performance of code-compliant steel special moment frames using ASCE 41-17. In: Structures. Vol. 54. Elsevier; 2023. p. 764–784.
18. Sae-Long W, Limkatanyu S, Prachasaree W, Horpibulsuk S, Panedpojaman P. Nonlinear Frame Element with Shear–Flexure Interaction for Seismic Analysis of Non-Ductile Reinforced Concrete Columns. International Journal of Concrete Structures and Materials. 2019;13(1):32. doi:10.1186/s40069-019-0343-2
19. Sae LW, Limkatanyu S, Hansapinyo C, Imjai T, Kwon M. Forced-based shear-flexure-interaction frame element for nonlinear analysis of non-ductile reinforced concrete columns. 2020.
20. Sae-Long W, Limkatanyu S, Panedpojaman P, Prachasaree W, Damrongwiriyanupap N, Kwon Mi, Hansapinyo C. Nonlinear Winkler-based Frame Element with Inclusion of Shear-Flexure Interaction Effect for Analysis of Non-Ductile RC Members on Foundation. Journal of Applied and Computational Mechanics. 2020 [accessed 2026 Aug 7];(Online First). https://doi.org/10.22055/jacm.2020.34699.2460. doi:10.22055/jacm.2020.34699.2460
21. Limkatanyu S, Sae-Long W, Damrongwiriyanupap N, Sukontasukkul P, Imjai T, Chompoorat T, Hansapinyo C. Nonlinear shear-flexure-interaction RC frame element on Winkler-Pasternak foundation. Geomechanics and Engineering. 2023;32(1):69–84. doi:10.12989/GAE.2023.32.1.069
22. Limkatanyu S, SaeLong W, Damrongwiriyanupap N, Imjai T, Chaimahawan P, Sukontasukkul P. Shear-Flexure Interaction Frame Model on Kerr-Type Foundation for

Analysis of Non-Ductile RC members on Foundation. Journal of Applied and Computational Mechanics. 2022 [accessed 2026 Aug 7];(Online First). https://doi.org/10.22055/jacm.2022.39597.3440. doi:10.22055/jacm.2022.39597.3440

23. Jalili J, Mahood M, Shafiee A. Evaluation of near-fault effects on the general code spectrum of the Iranian code of practice for seismic-resistant design of buildings, case study: Tehran. Journal of Seismology. 2022;26(6):1223–1244.
24. Suzuki A, Abe K, Suzuki K, Kimura Y. Cyclic Behavior of Perfobond-Shear Connectors Subjected to Fully Reversed Cyclic Loading. Journal of Structural Engineering. 2021;147(3):04020355. doi:10.1061/(ASCE)ST.1943-541X.0002955
25. Tripathi M, Dhakal RP, Dashti F. Nonlinear cyclic behaviour of high-strength ductile RC walls: Experimental and numerical investigations. Engineering Structures. 2020;222:111116. doi:10.1016/j.engstruct.2020.111116
26. Elwood KJ. Modelling failures in existing reinforced concrete columns. Canadian Journal of Civil Engineering. 2004;31(5):846–859.
27. Bae S. Seismic performance of full-scale reinforced concrete columns. The University of Texas at Austin; 2006.
28. Bentz E. Sectional analysis of reinforced concrete members. 2000.
29. Vecchio FJ, Collins MP. The modified compression-field theory for reinforced concrete elements subjected to shear. In: Journal Proceedings. Vol. 83. 1986. p. 219–231.
30. Soesianawati MT. Limited ductility design of reinforced concrete columns. 1986.
31. Zahn FA. Design of reinforced concrete bridge columns for strength and ductility. 1985.
32. Tanaka H. Effect of lateral confining reinforcement on the ductile behaviour of reinforced concrete columns. 1990.
33. Watson S. Design of Reinforced Concrete Frames. 1989.

34. Xiao Y, Martirossyan A. Seismic Performance of High-Strength Concrete Columns. Journal of Structural Engineering. 1998;124(3):241–251. doi:10.1061/(ASCE)0733-9445(1998)124:3(241)

35. Mostafaei H, Vecchio FJ, Kabeyasawa T. Deformation Capacity of Reinforced Concrete Columns. ACI structural journal. 2009;106(2):187.

36. Paulay T, Priestley MJN. Seismic design of reinforced concrete and masonry buildings. New York Chichester Brisbane [etc.]: J. Wiley & sons; 1992.

37. 318-19 Building Code Requirements for Structural Concrete and Commentary. American Concrete Institute; 2019. https://www.concrete.org/publications/internationalconcreteabstractsportal.aspx?m=details&ID=51716937. doi:10.14359/51716937

38. Jcss J. Probabilistic model code. Joint Committee on Structural Safety. 2001;601.

39. Aboutaha RS, Engelhardt MD, Jirsa JO, Kreger ME. Rehabilitation of shear critical concrete columns by use of rectangular steel jackets. Structural Journal. 1999;96(1):68–78.

40. Sheikh SA, Yau G. Seismic behavior of concrete columns confined with steel and fiber-reinforced polymers. Structural Journal. 2002;99(1):72–80.

41. Prakash Ss, Li Q, Belarbi A. Behavior of circular and square reinforced concrete bridge columns under combined loading including torsion. ACI Structural Journal. 2012;109(3):317–328.

42. Hadi MNS. Behaviour of FRP wrapped normal strength concrete columns under eccentric loading. Composite structures. 2006;72(4):503–511.

43. Shear Friction Tests with High-Strength Concrete. ACI Structural Journal. 2002 [accessed 2026 Aug 7];99(1). http://www.concrete.org/Publications/ACIMaterialsJournal/ACIJournalSearch.aspx?m=details&ID=11040. doi:10.14359/11040

44. Ozbakkaloglu T, Saatcioglu M. Seismic Behavior of High-Strength Concrete Columns Confined by Fiber-Reinforced Polymer Tubes. Journal of Composites for Construction. 2006;10(6):538–549. doi:10.1061/(ASCE)1090-0268(2006)10:6(538)

45. Guner S, Vecchio FJ. Pushover analysis of shear-critical frames: formulation. ACI Structural Journal. 2010;107(01):63–71.

46. Dan Palermo and Frank J. Vecchio. Compression Field Modeling of Reinforced Concrete Subjected to Reversed Loading: Formulation. ACI Structural Journal. 2003 [accessed 2026 Aug 7];100(5). http://www.concrete.org/Publications/ACIMaterialsJournal/ACIJournalSearch.aspx?m=details&ID=12803. doi:10.14359/12803

47. Yılmaz MO. Inverse Calibration of Confinement and Softening in RC Beam-Column Joints for Improved DSFM Predictions. Buildings. 2026;16(6):1157. doi:10.3390/buildings16061157

48. Sadeghi M, Poorahad P, Shiravand MR, Samimi K. Ensemble learning-based prediction of the backbone curve for corroded reinforced concrete columns using experimental database. Scientific Reports. 2026;16(1):9367. doi:10.1038/s41598-026-40488-5

49. Mehta V, Jang SH, Chey MH. Predictive framework for shear strength and failure modes of exterior reinforced concrete beam–column joints using machine learning. Structural Concrete. 2026;27(2):1549–1580. doi:10.1002/suco.70391

50. Cui M, Wang C, Chen C, Qiu H, Pan Y, Wang B. Seismic Deformation Capacity Prediction of Steel-Reinforced Concrete (SRC) Columns Based on Test Database and Machine Learning. Buildings. 2026;16(10):1891.

51. Xiao Z, Wang L, Huang R. Seismic performance of reinforced concrete beam column joints strengthened with ECC shells. Scientific Reports. 2026;16(1):8137. doi:10.1038/s41598-026-39753-4

APPENDIX

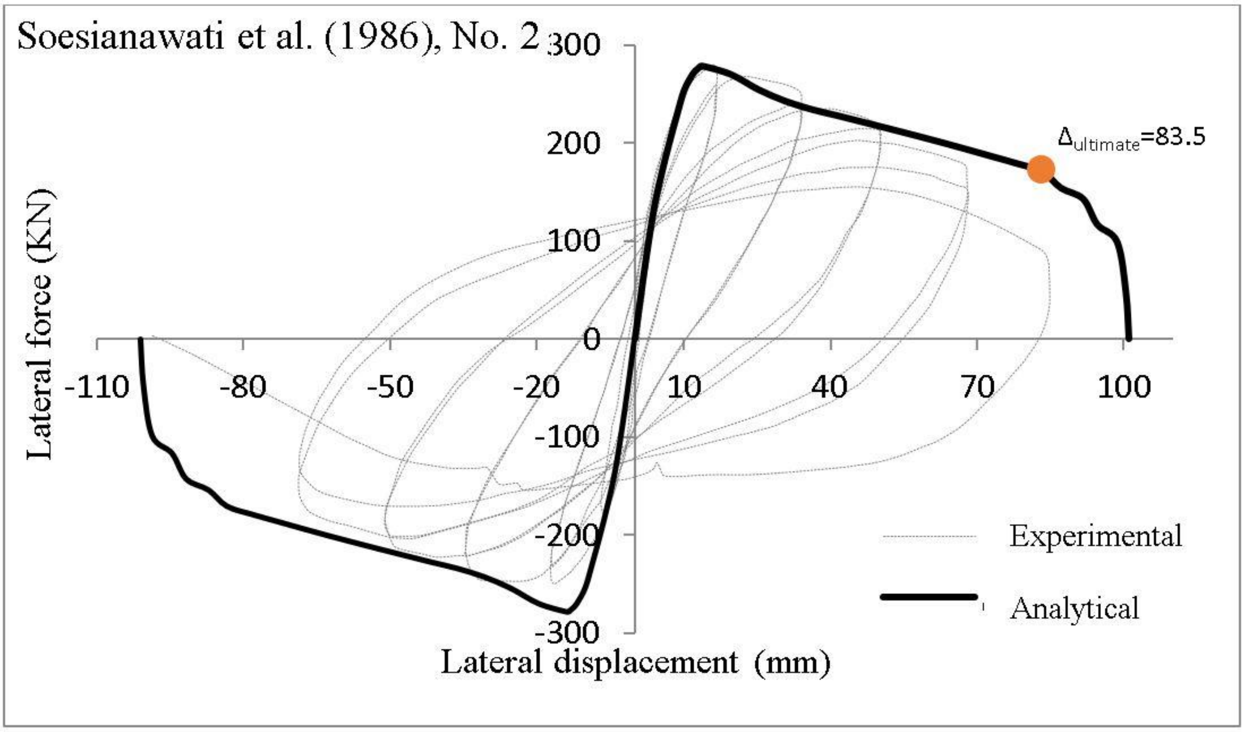
Soesianawati et al. (1986), No. 2
$\Delta_{ultimate}$=83.5
Lateral force (KN)
Lateral displacement (mm)
300
200
100
0
-100
-200
-300
-110
-80
-50
-20
10
40
70
100
Experimental
Analytical

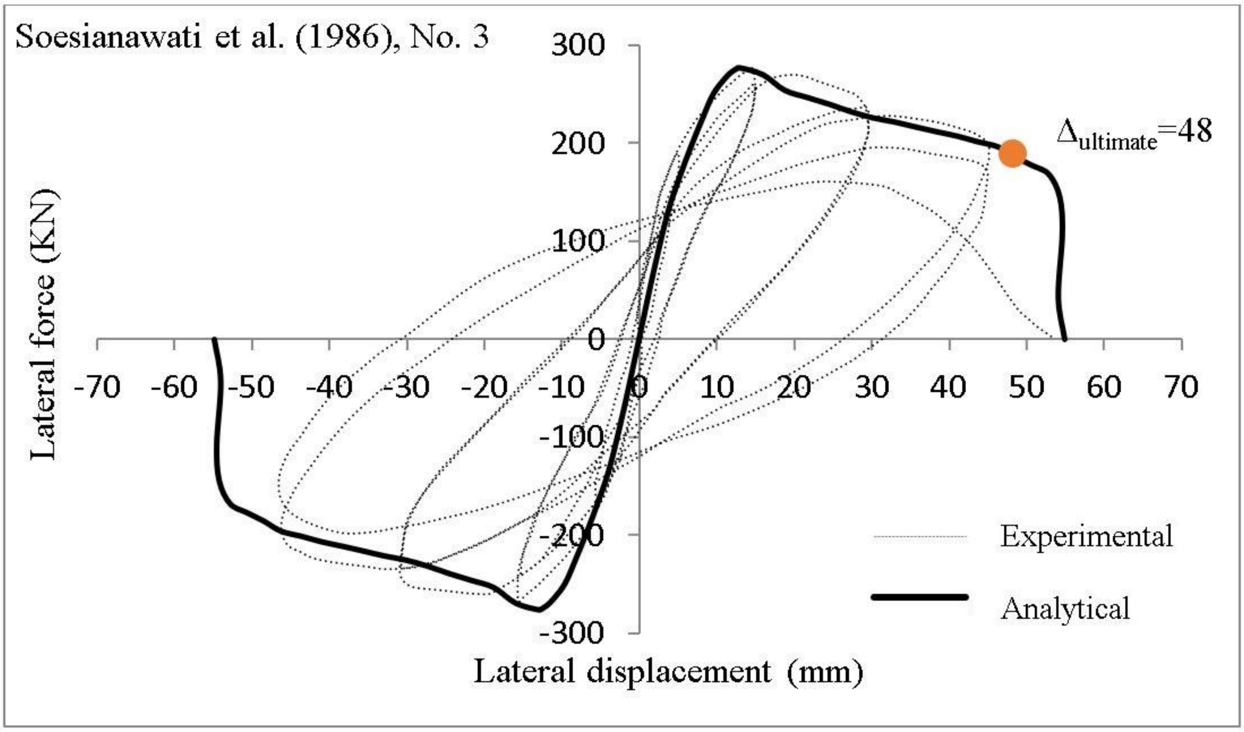
Soesianawati et al. (1986), No. 3
$\Delta_{ultimate}$=48
Lateral force (KN)
Lateral displacement (mm)
300
200
100
0
-100
-200
-300
-70
-60
-50
-40
-30
-20
-10
0
10
20
30
40
50
60
70
Experimental
Analytical

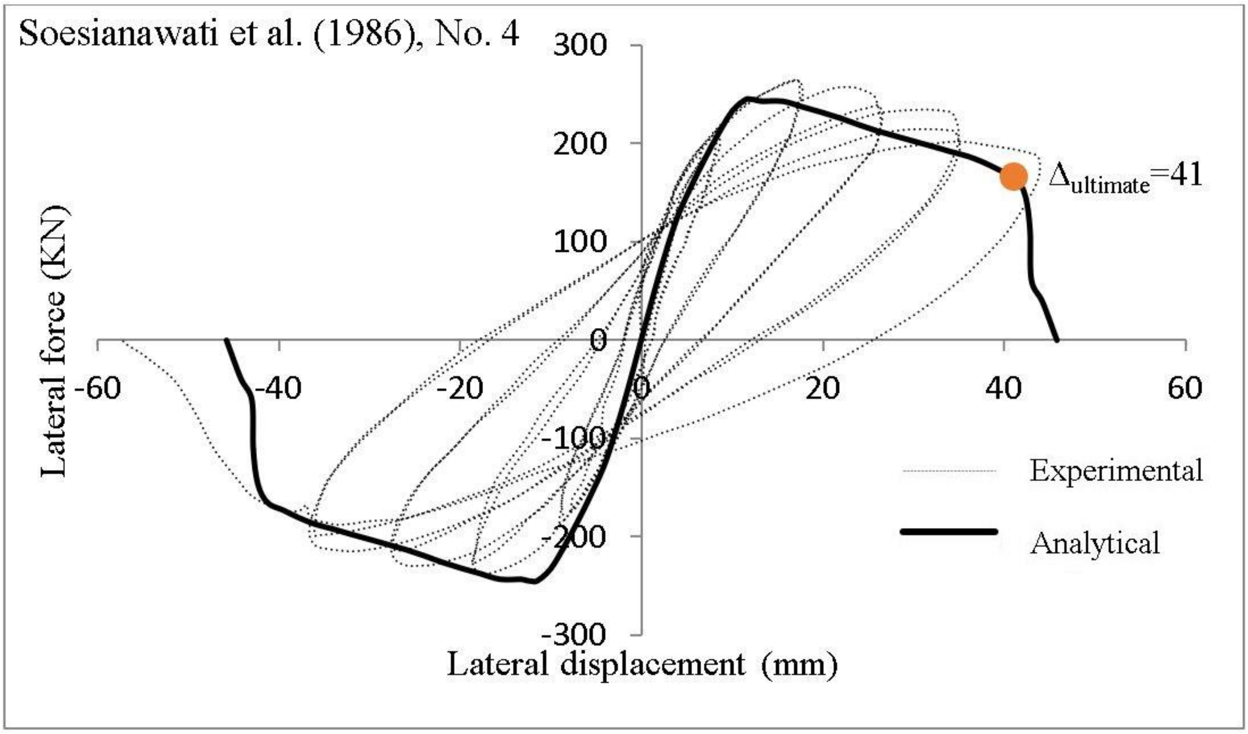
Soesianawati et al. (1986), No. 4
300
200
100
0
-100
-200
-300
-60
-40
-20
0
20
40
60
Lateral force (KN)
Lateral displacement (mm)
$\Delta_{ultimate}$=41
Experimental
Analytical

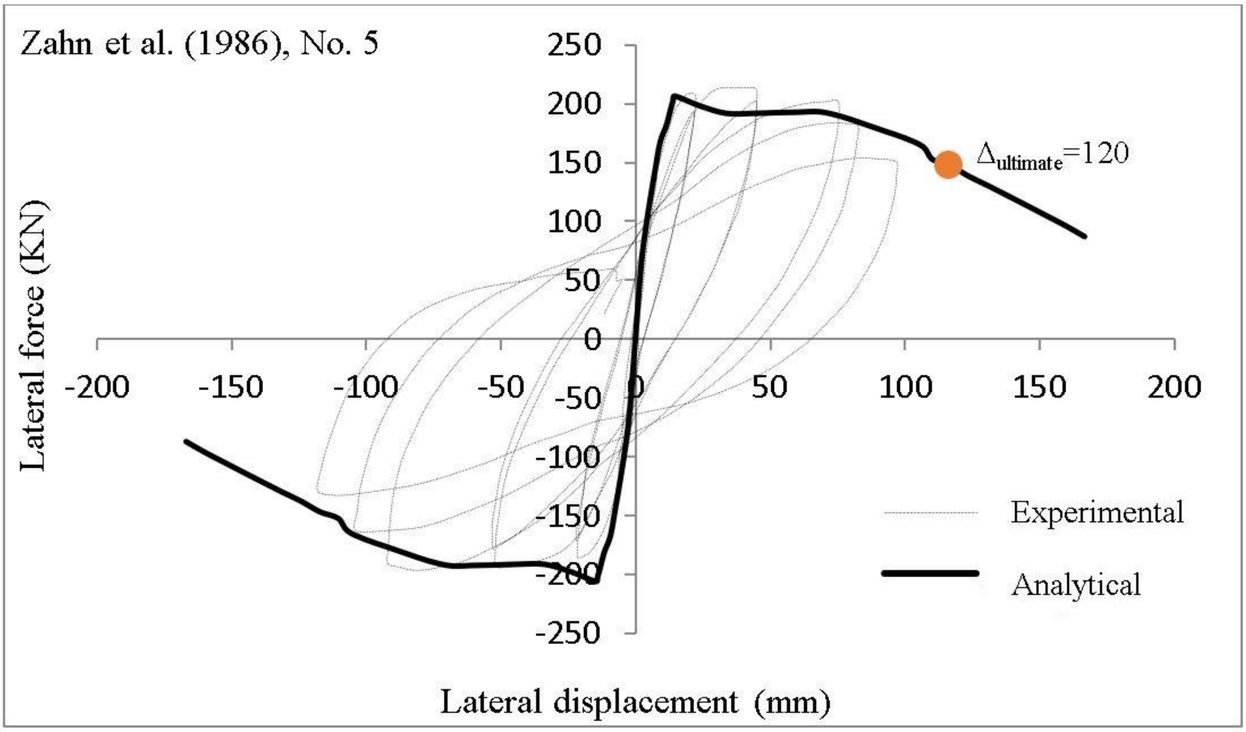
Zahn et al. (1986), No. 5
250
200
150
100
50
0
-50
-100
-150
-200
-250
-200
-150
-100
-50
0
50
100
150
200
Lateral force (KN)
Lateral displacement (mm)
$\Delta_{ultimate}$=120
Experimental
Analytical

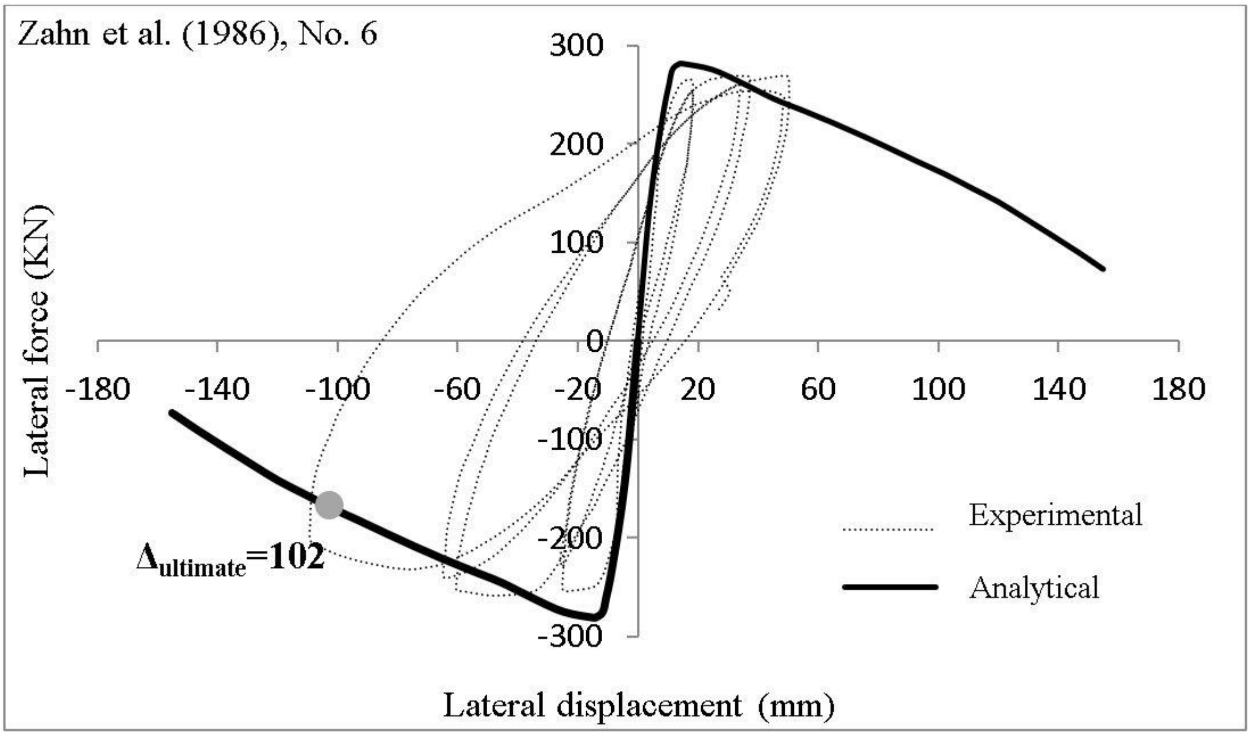
Zahn et al. (1986), No. 6
300
200
100
0
-100
-200
-300
-180
-140
-100
-60
-20
20
60
100
140
180
Lateral force (KN)
Lateral displacement (mm)
$\Delta_{ultimate}$=102
Experimental
Analytical

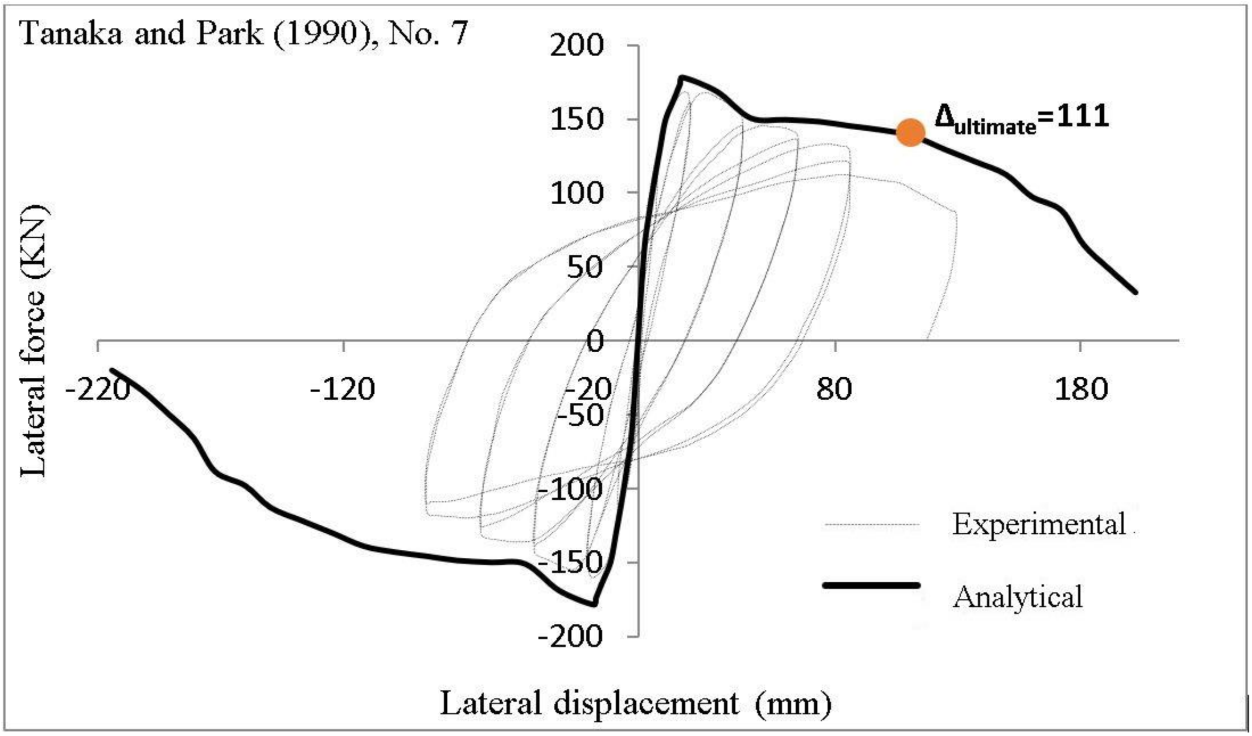
Tanaka and Park (1990), No. 7
200
150
100
50
0
-50
-100
-150
-200
-220
-120
-20
80
180
Lateral force (KN)
Lateral displacement (mm)
$\Delta_{ultimate}$=111
Experimental
Analytical

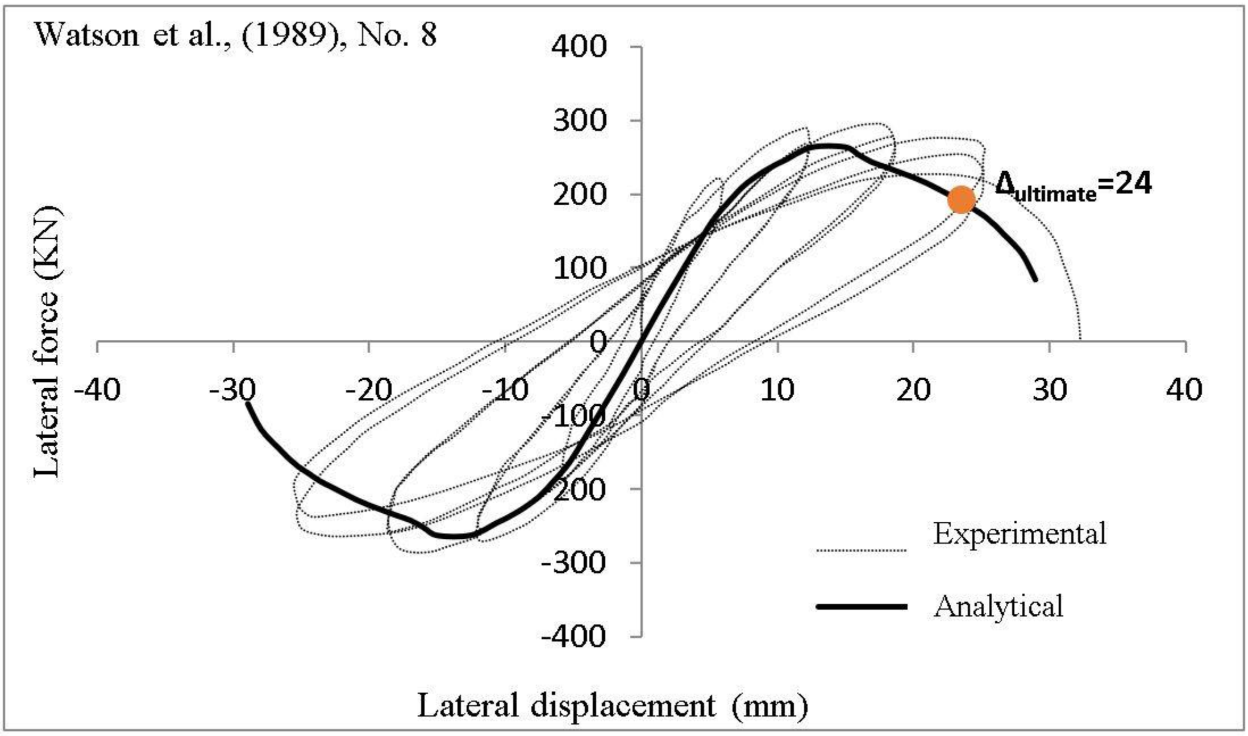
Watson et al., (1989), No. 8
Δultimate=24
Experimental
Analytical
Lateral force (KN)
Lateral displacement (mm)

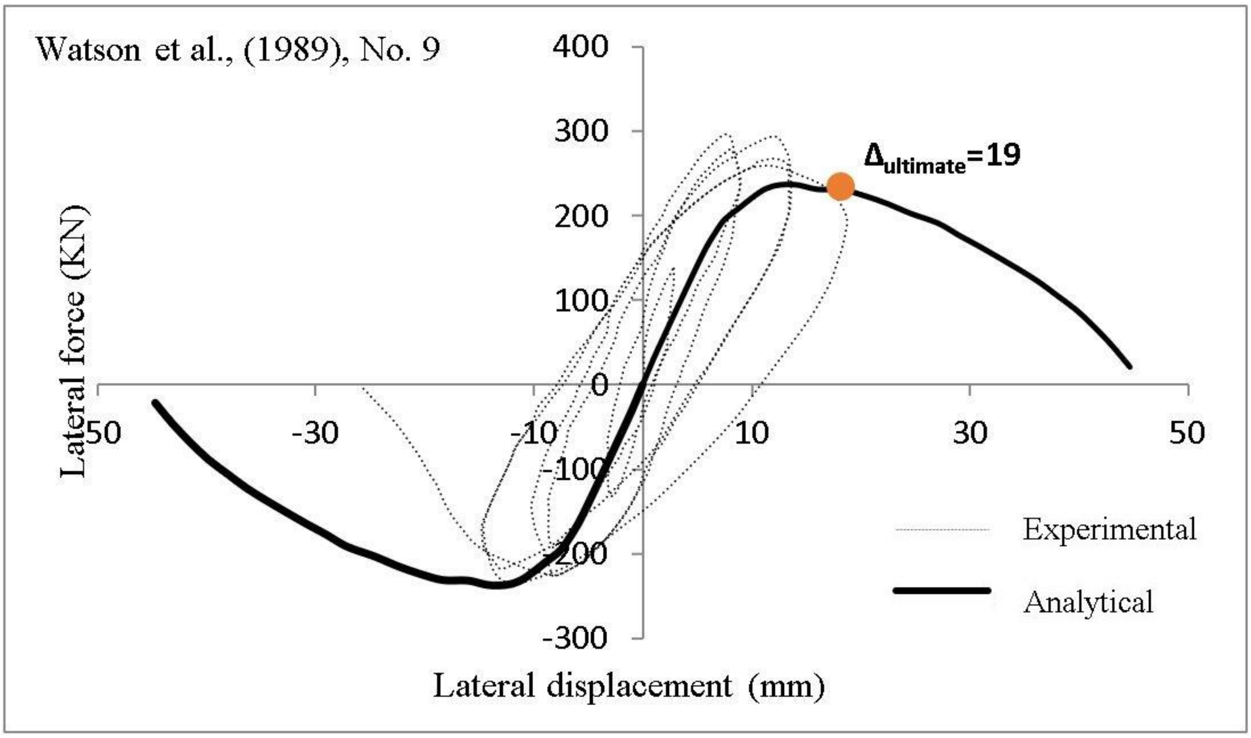
Watson et al., (1989), No. 9
Δultimate=19
Experimental
Analytical
Lateral force (KN)
Lateral displacement (mm)

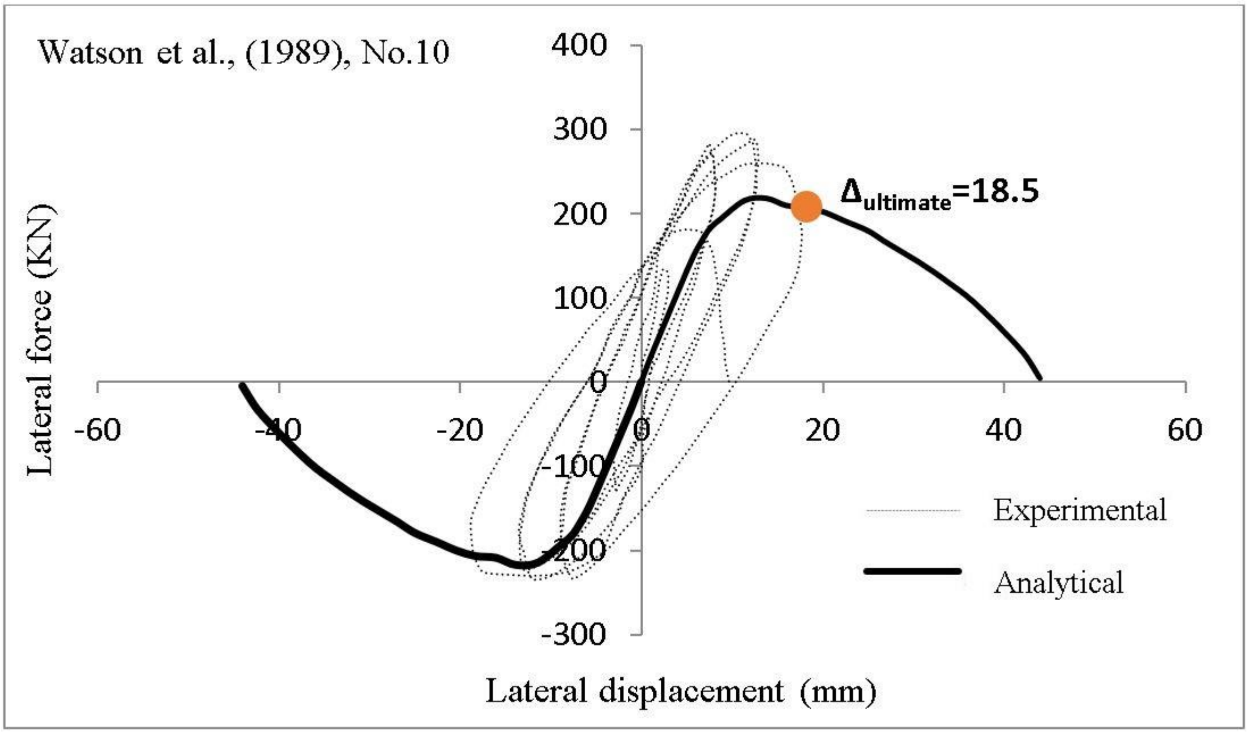
Watson et al., (1989), No.10
$\Delta_{ultimate}$=18.5
Lateral force (KN)
Lateral displacement (mm)
Experimental
Analytical
400
300
200
100
0
-100
-200
-300
-60
-40
-20
0
20
40
60

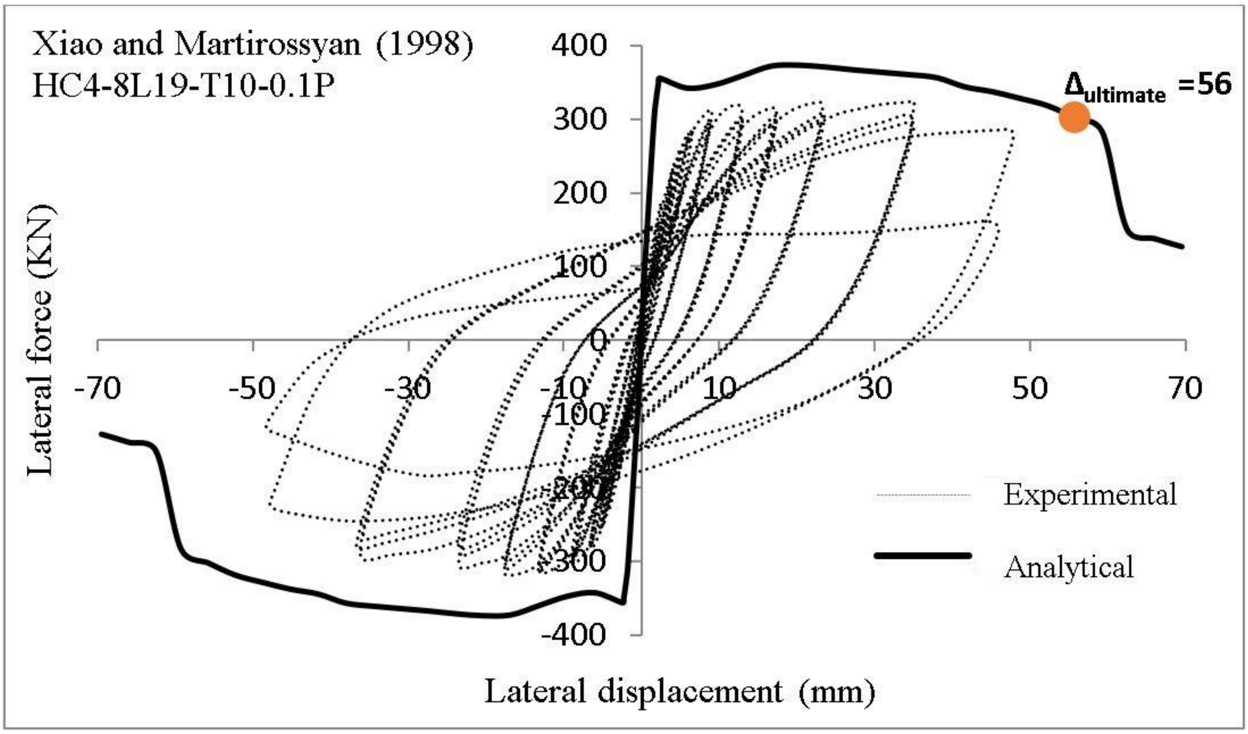
Xiao and Martirossyan (1998)
HC4-8L19-T10-0.1P
$\Delta_{ultimate}$ =56
Lateral force (KN)
Lateral displacement (mm)
Experimental
Analytical
400
300
200
100
0
-100
-200
-300
-400
-70
-50
-30
-10
10
30
50
70

SI 2:

A step-by-step solution to one example.

In this section, the ASFI method was implemented using Mathematica, and the results were verified against the example presented by Mostafaei et al (2009). While differences were observed in the intermediate components γf and γs, the computed total displacement ratio γ closely matched the reference result.

The analytical process for the sample concrete column is detailed below:

Specimen Name	b (mm)	h (mm)	Lin (mm)	Sh (mm)	ϱg (%)	ϱw (%)	fsyx (MPa)	fsyy (MPa)	fc' (MPa)	P (kN)
Mostafaei et al. 2009	300	300	900	150	2.26	0.14	415	410	28	540

1. Initial Concrete Compressive Strain (εc)

- Assumed: εc = -0.002

Determination of ε0 (Strain at Mid-section)

- Initial assumption: ε0 = 0.002
- Calculation of parameter a where a = 0.85C:

Eq. (1)

$$a = \frac{h\varepsilon_c}{2.353\varepsilon_c - 1.353\varepsilon_0} = \frac{300\times(-0.002)}{2.353\times(-0.002) - 1.353\times(0.002)} = 81\ \text{mm}$$

3. Axial strain at the inflection point, εxa, is calculated using the following equation:

Eq. (2)

$$\varepsilon_{xa} = \frac{\frac{P}{bh}}{2f_p/\varepsilon_p + E_s\rho_{xx}} = -0.00019$$

4. Mean principal compressive strain of concrete, ε2, and axial strain εx for the shear model are calculated as:

Eq. (3)

$$\varepsilon_2 = \frac{\varepsilon_c + \varepsilon_{xa}}{2} = -0.00101$$

$$\varepsilon_x = \frac{\varepsilon_0 + \varepsilon_{xa}}{2} = 0.0014$$

5. Assuming that the transverse reinforcement has yielded, the following equation can be used to calculate ε1:

Eq. (4)

$$\varepsilon_l = \frac{(\varepsilon_x - \varepsilon_2)(f_{c1} - f_{cx})}{f_{cl} + \rho_{sy} f_{syy}} + \varepsilon_x \quad \varepsilon_y \geq \varepsilon_{yy}$$

Eq. (5)

$$\sigma_x = \sigma_0 = \frac{p}{bh}, \quad f_{c1} = 0.44 f_y' = 0.44 \times 0.33\sqrt{f_c'} = 0.44 \times 0.33\sqrt{28} = 0.77 \text{ MPa}$$

Eq. (6)

$$\varepsilon_1 = 0.024$$

6. To calculate tanθc (crack angle), use the following equation:

Eq. (7)

$$\tan^2 \theta_c = \frac{\varepsilon_x - \varepsilon_2}{\varepsilon_y - \varepsilon_2} \rightarrow \tan \theta_c = 0.33$$

7. Using the following equation to check for shear failure.

Eq. (8)

$$\tau_f = \frac{M}{bd_f L_{in}} = \frac{1.26 \times 10^8}{300 \times 260 \times 450} = 3.59 \geq \tau_i + f_{syy} \rho_{sy} \cot \theta = 2.17$$

The result shows that a shear failure has occurred. If the above relationship was not satisfied, εc should be reduced until the relationship is met with the identified value.

8. Using the following equation, the ultimate displacement ratio (γ) is calculated:

Eq. (9)

$$\gamma_f = \frac{\delta}{L_{in}} = \frac{1}{L_{in}} \int_0^{L_{in}} x\phi dx = 0.002$$

$$\gamma_s = \frac{2(\varepsilon_x - \varepsilon_2)}{\tan\theta_c} = 0.0029$$

$$\gamma = \gamma_f + \gamma_s = 0.0049$$